Bulletin of the Seismological Society of America, Vol. 108, No. 2, pp. 553–572, April 2018, doi: 10.1785/0120170139

Resolving Source Geometry of the 24 August 2016 Amatrice, Central Italy, Earthquake from InSAR Data and 3D Finite-Element Modeling

by Sui Tung and Timothy Masterlark

Abstract The source geometry of the 24 August 2016 Amatrice earthquake is studied with Sentinel 1-A/B and Advanced Land Observation Satellite (ALOS)-2 Interferometric Synthetic Aperture Radar (InSAR) coseismic observations. Without presetting the fault geometry and location, we allow these geodetic data to constrain a planar fault and a listric dislocation through an innovative nonlinear approach. Finite-element models (FEMs) are built to simulate the earthquake deformation over a domain with a distribution of realistic crustal materials. Optimal fault geometries are resolved with the observed coseismic displacements in both homogeneous (HOM) half-spaces and heterogeneous (HET) FEMs. The HET-computed planar slip is modeled next to the hypocenter and estimated with a very compatible dip (47°) similar to the moment tensor solution, while that of the HOM solution is offset by ~14°. Meanwhile, the former recovers the coseismic displacements significantly better than the latter at 95% confidence. This indicates that the inverse solutions of source analysis are sensitive to the presence of nonuniform rock materials in the elastic domain. Though abundant fault detachments are documented within the epicentral area, the slip distributions derived along optimized listric faults do not improve the prediction of surface movements estimated by the rectangular sources. This implies that a planar fault geometry is sufficient to describe the rupture of the Amatrice earthquake. The corresponding slip distribution reveals a maximum slip of ~1 m at 7 km depth, beneath a lithological boundary between the shallow weaker units and the underlying stronger Dolomite. A significant correlation is found between the slip magnitude and subsurface rock stiffness where stress is being accumulated, implying a possible structural control on the earthquake nucleation and propagation.

Introduction

The central Mediterranean region has been seismically active, due to the continuous northward convergence (~5–6 mm/yr) between the Eurasian plate and African (Nubia) plate along a complex plate margin (Reilinger *et al.*, 2006; Serpelloni *et al.*, 2007). The present-day seismotectonics of central Italy are further complicated by the anticlockwise rotation and flexural hinge retreat of the Adria plate with respect to the Eurasian plate, as well as by the back-arc opening of the Tyrrhenian Sea, resulting in the current northeast–southwest extension along the axial belt of the plate periphery (Westaway, 1990; Morelli and Boschi, 1998; Nocquet, 2012). Despite the coexisting crustal shortening, this extensional field continues to stretch the Apennines belt in an east–west direction and create extensive north–south-trending normal-fault systems along the mountain ranges, causing significant earthquake events (M_w 3.8–6.3) over the past few decades (Margheriti *et al.*, 1998; Ciaccio *et al.*, 2005; Ameri *et al.*, 2009; Cirella *et al.*, 2009; Marzorati *et al.*, 2014; Albano *et al.*, 2015).

On 24 August 2016, an M_w 6.2 earthquake (42.723° N, 13.188° E) occurred near (<2 km) Accumoli and 10 km northwest (NW) of Amatrice, central Italy (Anzidei and Pondrelli, 2016; U.S. Geological Survey [USGS], 2016; see Data and Resources), as shown in Figure 1. This strong event (hereafter, the Amatrice earthquake [AE]) ruptured a broad section (~50 km) of the central Apennines that is a part of the accretionary prism of the subduction boundary between the overriding Eurasian plate and the subducting Adria plate. The hypocenter is located at a shallow depth (~8 km; Scognamiglio *et al.*, 2016) in proximity to the north-northwest (NNW)-striking Vettore fault (VF) and the Gorzano fault (GF) system, for which the (extensional) tectonic activities (~1.5 mm/yr) were examined by various field studies (Calamita and Pizzi, 1992, 1994; Pizzi *et al.*, 2002; Galadini and Galli, 2003). Surface offsets were observed along the southern section of the VF and the northern section of the GF (Livio *et al.*, 2016; Pucci *et al.*, 2017). These fault systems are parallel to the ranges of Mt. Vettore and Laga

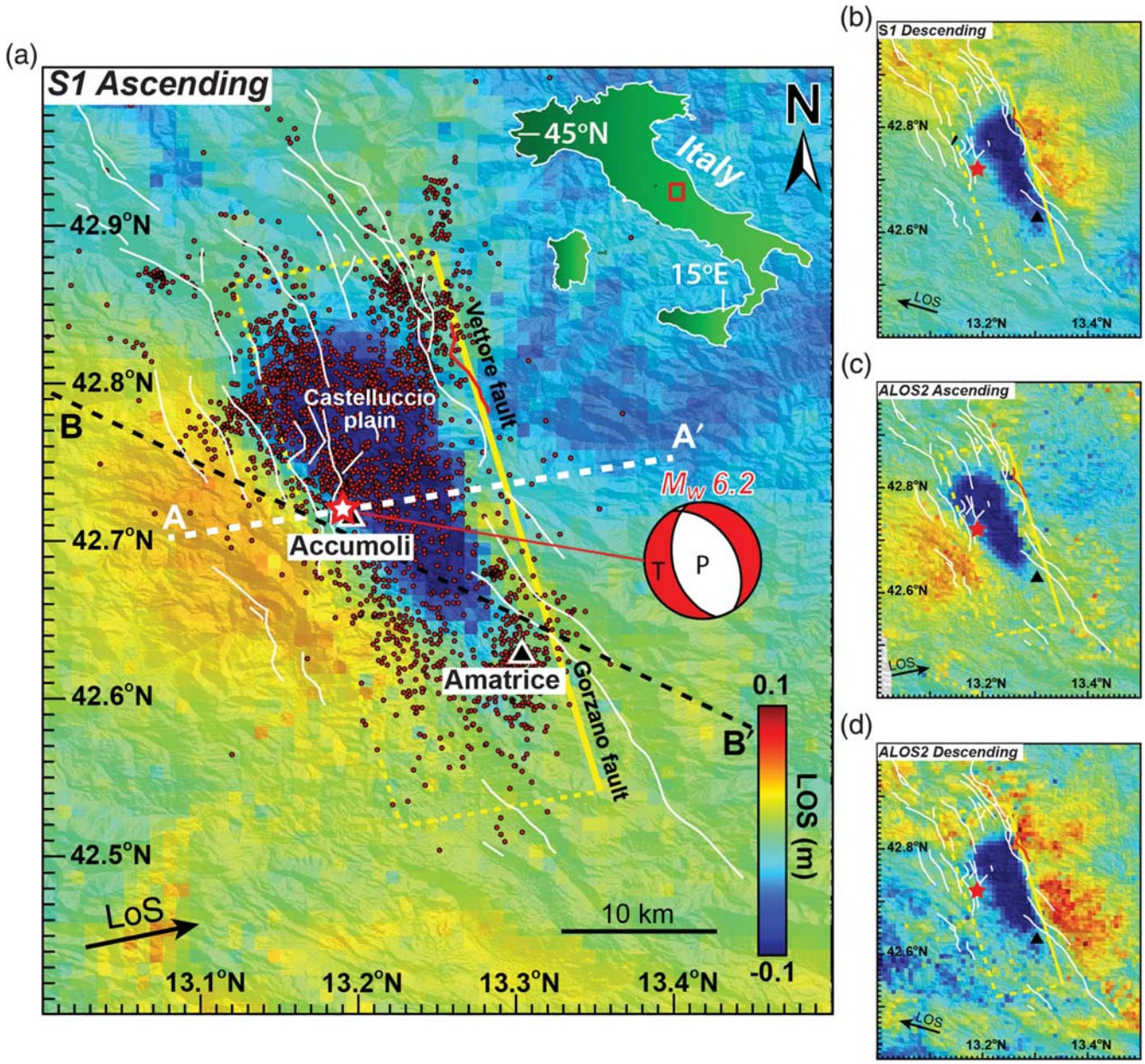

Figure 1. Tectonic setting and coseismic surface displacements of the Amatrice earthquake (AE). The focal mechanism represents a north–south-trending normal faulting of the mainshock (U.S. Geological Survey [USGS], 2016). Near-field line of sight (LoS) displacements are revealed by both (a,b) Sentinel 1-A/B and (c,d) Advanced Land Observation Satellite (ALOS)-2 Interferometric Synthetic Aperture Radar (InSAR) data spanning between 9 September 2015 and 31 August 2016 (Huang *et al.*, 2017). Red solid line is the AE-associated surface offset observed along the southern Vettore fault (Pucci *et al.*, 2017). The yellow line represents the finite-fault geometry resolved by Huang *et al.* (2017). Thin white solid lines indicate the active faults in the central Apennines. Near-field aftershocks occurring within 21 days after the mainshock are displayed as red dots. (a) The red box at the top right inlet shows the map location.

Mountains, intersecting the mountainous areas and the nearby alluvial graben basins (Galadini and Galli, 2003). Paleoseismological analyses suggest that earthquakes with M_w 6.5–6.6 have activated these fault systems (Galadini and Galli, 2003). For the AE, preliminary seismological models and moment tensor solutions indicate predominantly normal faulting plus minor left-lateral strike slip along a west-dipping fault with strike/dip/rake of 165°/49°/−78° from USGS and 142°/45°/−106° from Global Centroid Moment Tensor. The strong ground motion destroyed more than half of the town of Amatrice, with a combined death toll of ∼300 (BBC, 2016). Aftershocks of magnitudes between 2 and 5.35 continued for weeks after the mainshock (Michele *et al.*, 2016) within the seismic gap between the recent 2009 M_w 6.3 L'Aquila earthquake (Atzori *et al.*, 2009) and the 1997 M_w 5.7 Colfiorito earthquake (Stramondo *et al.*, 1999). Two strong earthquakes of M_w 6.1 and 6.6 struck the same area near Visso and Norcia on 16 and 30 October 2016,

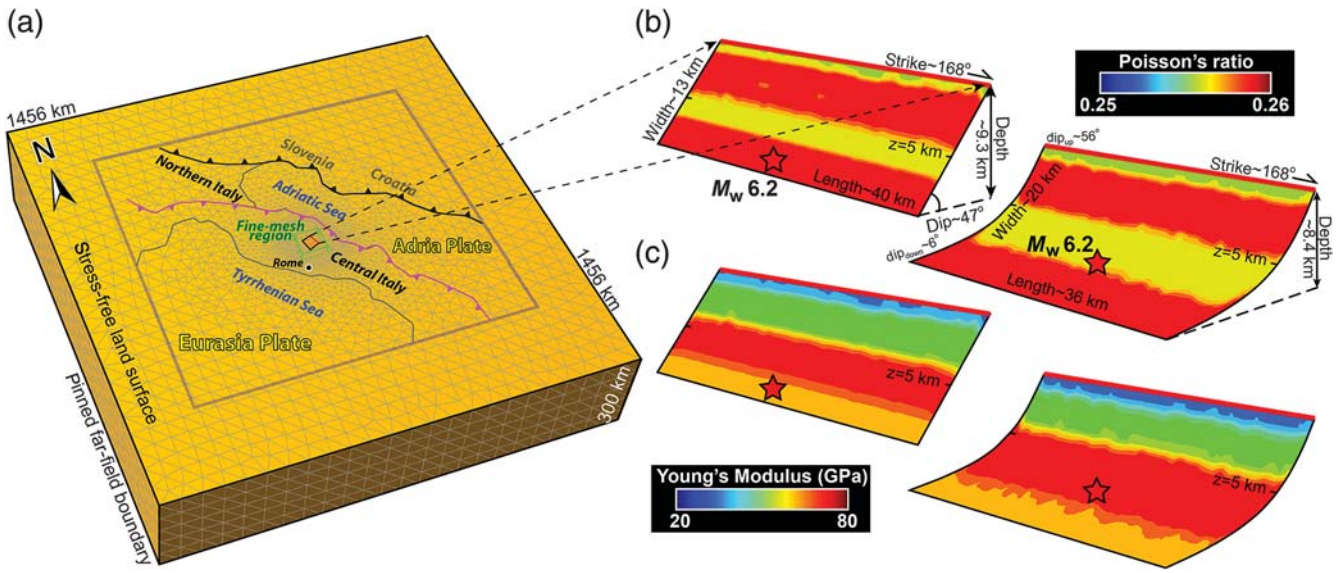

Figure 2. Finite-element model (FEM) simulating coseismic dislocation in a 3D heterogeneous domain. (a) FEM domain accommodates crustal entities of the subduction zone in the central Mediterranean. The domain approximates a block with dimensions of $1456 \times 1456 \times 300$ km^3. The domain top is a stress-free surface representing the land and seafloor surfaces. A fine-mesh region (green box) specifies the near-field tectonics and contains a structural discontinuity (either a rectangular or listric fault) that hosts the seismic rupture. (b) The distribution of Young's modulus and (c) Poisson's ratio are derived from the regional velocity model by Cirella *et al.* (2012) and CRUST2.0 (Bassin, 2000). Near-field rock strength increases abruptly at a depth of ~4 km as Young's modulus increases from ~55 to 85 GPa.

respectively, implying complex seismic sequences (Cheloni *et al.*, 2017). In this work, our study focuses on investigating the 24 August 2016 AE.

There is a long-standing controversy between the manifestations of planar and listric rupture during earthquakes, which is not trivial in complex tectonic settings, such as accretionary prisms, orogenic belts, and subductive margins. In orogenic environments such as central Italy, listric faults are common, due to the coexistence of detachment faulting and basal decollements (Bigi *et al.*, 2003; Tao *et al.*, 2015; Borghi *et al.*, 2016; Lavecchia, Adinolfi, *et al.*, 2016). The refined aftershock locations show that the majority of aftershocks following the AE clustered within the Castelluccio plain at depths of 5–12 km (Fig. 1) and corroborate extensive gently dipping structures (Chiaraluce *et al.*, 2017). These low-angled structures are supported by the field evidence of listric faults connected to decollements at 6–10 km depth (Calamita and Pizzi, 1994; Bigi *et al.*, 2003; Borghi *et al.*, 2016), comparable with the listric rupture of the 2009 L'Aquila earthquake to the south (Borghi *et al.*, 2016; Lavecchia, Adinolfi, *et al.*, 2016). Several planar finite-fault models were estimated for the AE (Lavecchia, Castaldo, *et al.*, 2016; Tinti *et al.*, 2016; Cheloni *et al.*, 2017; Huang *et al.*, 2017). However, Huang *et al.* (2017) argue that a rectangular source might not be able to describe the very near-field displacements related to shallower fault slip if the actual fault is listric. Because flat decollements are generally interpreted along the root of VF and GF near the AE epicenter (Bigi *et al.*, 2009), such as other detachment fault networks within the central Apennines, the AE becomes a good candidate for the test of a listric earthquake source furnishing the existing uniform-dipping models. By comparing the slip models of different fault configurations, our analysis serves to test the hypothesis that the planar fault approximation is sufficient to describe the seismic rupture of the AE.

Moreover, the near-field foreland basin system (Laga basin) near the AE consists of pelagic, turbiditic, and carbonate platform deposits, and clastic foredeep sediments (Bigi *et al.*, 2003). Figure 2b,c shows a weaker layer superimposed with the sedimentary sequence between 0 and 4 km revealed by seismic tomography (Li *et al.*, 2007; Scarfì *et al.*, 2009) and velocity models (Cirella *et al.*, 2012). Even without extensive surface cracking, this subsurface layer of soft materials, to some extent, can amplify seismic shear waves and thus encourage stronger ground shaking (Chau and Lo, 2001), explaining the destructiveness of past earthquakes along the Apennines mountain belt. It is also well known that such subsurface material heterogeneity controls how fault slip is translated into surface displacements during earthquakes (Sato, 1971; Jovanovich *et al.*, 1974; Savage, 1987, 1998; Fernandez *et al.*, 1996; Pan, 1999; Masterlark *et al.*, 2001, 2012; Eleonora *et al.*, 2002; He *et al.*, 2003; Hearn and Bürgmann, 2005; Wang *et al.*, 2006; Trasatti *et al.*, 2011; Williams and Wallace, 2015), to which the solutions of inverse analyses are sensitive. In central Italy, the complex configurations of crustal materials pose a fundamental challenge to geodetically invert for seismic sources using customary models that simulate dislocation in a homogeneous half-space, which would either overestimate or underestimate slip in weak and rigid zones, respectively (Masterlark *et al.*,

2012; Tung and Masterlark, 2016). Hence, simulating distributed rock properties in deformational models might become essential for a more accurate estimation of coseismic slip distributions (e.g., Masterlark, 2003; Hughes *et al.*, 2010; Kyriakopoulos *et al.*, 2013; Tung and Masterlark, 2016). Furthermore, the material heterogeneity further affects the calculation of *in situ* Coulomb stress and thus the prediction of aftershock-prone areas (He *et al.*, 2003; Hearn and Bürgmann, 2005). Therefore, we construct finite-element models (FEMs) of deformation with distributed rock materials to study the source geometry of the AE.

The goals of this work are to compare the seismic source of the AE resolved over a planar fault and a listric fault geometry and test the corresponding solution sensitivity toward the nonuniformity of rock materials in the upper crust. As constrained by coseismic Interferometric Synthetic Aperture Radar (InSAR) observations (Fig. 1), these geometries are first retrieved through nonlinear analyses and then used for linearly deriving the detailed slip distribution. More realistic representations of the Green's function matrices are generated through FEMs that assemble the regional tectonic environment of the central Mediterranean (Fig. 2). FEMs are, so far, the best tool for simulating elastic dislocation within a velocity-constrained rock heterogeneity (Masterlark and Hughes, 2008) and are proved to provide more accurate predictions of coseismic displacements than the conventional analytical solutions (Tung and Masterlark, 2016). Our rapid FEM generation technique (build time < 10 min for each FEM) enables sampling over thousands of high-resolution FEMs for the optimal source geometry, through effective algorithms and computational parallelization. Hence, this study serves as a pioneer to conduct a nonlinear source analysis in an inhomogeneous crustal domain (compare to Huang *et al.*, 2017), which cannot be accomplished by the analytical models of faults embedded in isotropic half-spaces (e.g., Okada, 1985). The resolved fault geometries and the corresponding slip models are then studied in the context of the local rock stiffness for possible structural control over the earthquake.

Methods

InSAR Data

The coseismic deformation was captured by multiple pairs of satellite Synthetic Aperture Radar (SAR) images with different acquisition dates (Lavecchia, Castaldo, *et al.*, 2016; Huang *et al.*, 2017). The surface subsided by up to 20 cm near Accumoli and uplifted as much as 9 cm along the down-dip edge of the fault (Lavecchia, Castaldo, *et al.*, 2016; Huang *et al.*, 2017). In this work, we adopt the InSAR data processed by Huang *et al.* (2017) to re-analyze the seismic rupture of the AE. Both the ascending and descending tracks of Sentinel 1-A/B and Advanced Land Observation Satellite (ALOS)-2 are used to constrain the coseismic surface displacements (Fig. 1). The unwrapped images altogether consist of 17,701 pixels and cover an $\sim 70 \times 50$ km area surrounding the epicenter, with a horizontal resolution of 30 arcsec. The details of the interferograms are described in table S1 of Huang *et al.* (2017). The incidence angle of these four InSAR images $d_{\mathrm{S1_ASC}}$ (S1 ascending), $d_{\mathrm{S1_DES}}$ (S1 descending), $d_{\mathrm{ALOS2_ASC}}$ (ALOS2 ascending), and $d_{\mathrm{ALOS2_DES}}$ (ALOS2 descending) are of 34°–45° from vertical, so that the line of sight (LoS) displacements are more sensitive to the vertical ground movements. All LoS vectors roughly point along the east–west direction. The prominent ground depression found in two NW-southeast (SE)-striking deformation lobes could be the result of either two distinct sources or continuous rupture propagation over a single fault (Lavecchia, Castaldo, *et al.*, 2016). Collectively, these deformation signatures support a NW-trending west-dipping normal rupture that is in general agreement with the recent fault activities of the central Apennines (Calamita and Pizzi, 1994; Borghi *et al.*, 2016).

Finite-Element Models

A new generation of FEMs is employed to simulate the geological complexity of central Italy. Our FEMs, which are constructed within a commercial finite-element code Abaqus (see Data and Resources), inherit a 3D elastic domain with nonuniform crustal materials surrounding the epicentral area, as shown in Figure 2. The distribution of material properties in the central Mediterranean region is estimated from the global velocity model CRUST2.0 (Bassin, 2000; see Data and Resources), while the near-field materials are furthered refined with the regional model suggested by Cirella *et al.* (2012). Within the Abaqus-based FEM domain, the distributed rock properties are specified by spatially varying Young's modulus E and Poisson's ratio ν, which are respectively determined by

$$E = \frac{\rho V_S^2 (3V_P^2 - 4V_S^2)}{V_P^2 - V_S^2}, \tag{1}$$

$$v = \frac{V_P^2 - 2V_S^2}{2(V_P^2 - V_S^2)}, \tag{2}$$

in which V_P, V_S, and ρ refer to the P-wave velocity, S-wave velocity, and density, respectively. The shear modulus can be further formulated by $G = E/2(1 + v)$. The elastic dislocation is simulated in the Abaqus-standard module and governed by the equations of elasticity (e.g., Vasco *et al.*, 2002).

The domains of the FEMs are represented by a block centered at (42.707° N, 13.176° E) with 1456 km in width or length and 300 km in thickness (Fig. 2a). The domains comprise 30,000–80,000 nodes and 100,000–400,000 of first-order tetrahedral elements with element intensity gradually dropping away from the domain center (Table 1). The meshing scheme is a nonstructural aggregation implemented through the Abaqus–Complete Abaqus Environment (CAE)

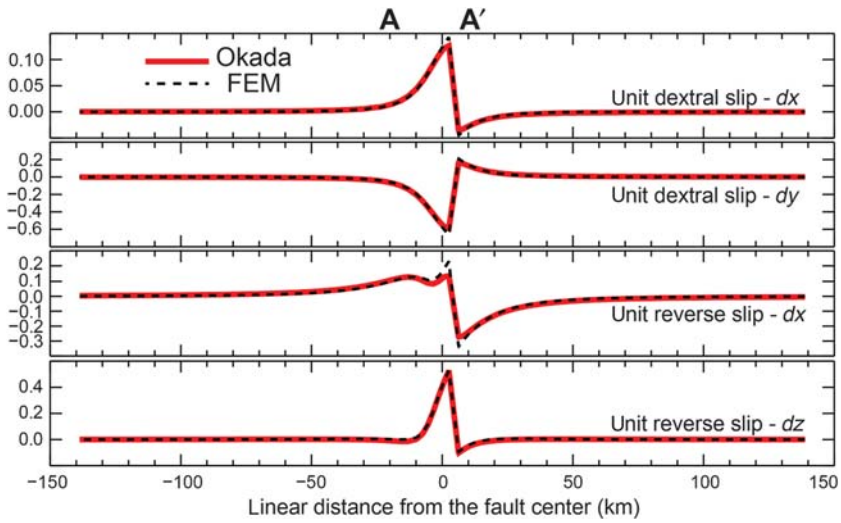

Figure 3. FEM validation. Predicted deformation of unit-dextral and unit-thrust slip by an FEM (homogeneous material) are validated against the analytical model in a half-space (Okada, 1985) along a fault-perpendicular profile AA′ shown in Figure 1.

module. The fault rupture is embedded in a designated fine-mesh region (FMR; width 125 km, length 125 km, and depth 40 km) for a refined near-field resolution (Fig. 2a). The elements exhibit characteristic lengths of 1 km on the fault surface, 2 km on the rims of FMR, and 120 km along the far-field boundaries. A total of 450–665 subpatch node pairs are configured on the fault surface for simulating the seismic rupture. The elastic dislocation is formulated through the kinematic constraint equations among these subpatch node pairs (Masterlark, 2003), and the details are discussed in the Kinematic Constraint of Elastic Dislocation section. The outer surfaces of the block represent the far-field lateral and depth boundary of the domain, with zero-displacement boundary conditions. These surfaces are separated from the fault center by a distance at least 10 times longer than the fault dimension to ensure the calculation consistency with the analytical solutions (Fig. 3). The domain top is a stress-free surface corresponding to the land and seafloor surface. The details of model specifications are described in Table 1.

Kinematic Constraint of Elastic Dislocation

The fault dislocation in FEMs is configured by the kinematic constraints developed by Masterlark (2003). The fault discontinuity in FEM is composed of multiple node pairs in which each pair consists of two overlapping nodes sharing the same initial location. A static fault slip is applied to these node pairs by relatively offsetting the two node members, nodes $n1$ and $n2$ of each pair, along the rake θ_{rake}. The kinematic constraints specify a relative fault offset Δu of each node pair through three equations of motion along orthogonal axes:

$$u^{n1}_{\text{strike}} - u^{n2}_{\text{strike}} = \Delta u_{\text{strike}} = \Delta u \times \cos(\theta_{\text{rake}}), \tag{3}$$

$$u^{n1}_{\text{dip}} - u^{n2}_{\text{dip}} = \Delta u_{\text{dip}} = \Delta u \times \sin(\theta_{\text{rake}}), \tag{4}$$

$$u^{n1}_{\text{normal}} - u^{n2}_{\text{normal}} = 0, \tag{5}$$

in which u^{n1}_{strike} and u^{n2}_{strike} are the along-strike displacements of nodes $n1$ and $n2$, respectively; u^{n1}_{dip} and u^{n2}_{dip} are the along-dip displacements of nodes $n1$ and $n2$, respectively; and u^{n1}_{normal} and u^{n2}_{normal} are the fault-normal displacements of nodes $n1$ and $n2$, respectively. The null fault-normal displacements of equation (5) ensure the hanging block and foot block are welded together during the dislocation. Nonslipping node pairs are configured with $\Delta u = 0$ equivalent to a welded condition. For the FEM of a listric fault, 665 node pairs are assigned to assemble the fault so that the kinematic constraints contain ~2000 equations of motion. The predicted surface deformation of elastic dislocation from the above configurations has been verified against the half-space analytical solutions (Okada, 1985) in a homogeneous domain (Fig. 3).

Listric Fault Geometry

The listric fault geometry can be described explicitly by several types of formulation, such as power-law (Hutton *et al.*, 2001) and trigonometric equations (Tao *et al.*, 2015). In this study, we configure the listric curvature by the following shape function of depth:

$$z = \frac{2a}{\pi} a \tan\left(\frac{x}{b}\right) \tag{6}$$

(Tao *et al.*, 2015), in which z is the depth of the fault (always positive); x is the horizontal distance from the surface trace; and a and b are the geometric parameters controlling the listric curvature. This formula was adopted to simulate the listric rupture of the 2008 M_w 8 Sichuan earthquake, China (Tao *et al.*, 2015). A larger value of parameter a gives rise to a flatter fault, whereas a larger value of parameter b increases the wavelength of the curve. For simplicity, a single buried patch conforming to the above-shaped function is focused in accordance with the assumptions made by Lavecchia, Castaldo, *et al.* (2016) and Huang *et al.* (2017). Because only limited surface breaking is observed, we presume a fault locking depth D_m limiting the top of the fault below the surface and a horizontal fault width H_x referring to the horizontal distance between the lower fault edge and the surface trace (Fig. 1). The listric patch is assigned a length L, and the center of the surface trace is denoted as $[x_c, y_c]$. We assume that the curved fault shares the same surface trace and strike ϕ as the optimal planar fault solution, such that y_c is a linear function of x_c. As a whole, the listric fault geometry is constrained by a set of six parameters $[a, b, D_m, H_x, L, x_c]$ and estimated through a nonlinear inverse analysis. We

Table 1
Finite-Element Model (FEM) Configurations and Rock Material Specifications

FEM Parameters	Configurations and Specifications
Dimension of FEM domain	1456 × 1456 × 300 km (width × length × depth)
Dimension of FMR domain	125 × 125 × 40 km (78 × 78 × 40 km)
Center of FEM domain	[13.176° E, 42.707° N] [350622.21 m E, 4729891.5 m N, 0 m] (UTM zone 33)
Number of nodes	Planar: 28,276; listric: 78,552
Number of elements	Planar: 155,230; listric: 444,785 (first-order tetrahedral)
Initial conditions	Zero displacement in the entire model (equilibrium)
Listric fault geometry	14×40 km^2; strike = 168°; 6° < dip_{mean} = 27.8° < 56°
Planar fault geometry	20 × 36 km; strike = 168°; dip = 47°
Number of subfault patches	Planar: 450; listric: 665
Dimension of a subfault patch	1 km
Analysis types	Static elastic
Top boundary conditions	Stress-free surface
Far-field boundary conditions	Zero displacements along lateral and basal surface
HET material definition	Velocity models based on Bassin (2000) and Cirella *et al.* (2012)
HOM material definition	Westerly granite, [v, E] = [0.25, 37.5 GPa] (Wang, 2000)

FMR, fine-mesh region; HET, heterogeneous; HOM, homogeneous.

limit the search ranges of these parameters in accordance with the listric structures interpreted from seismic tomography and field observations. These parameters are not designed to recover a curvature-free planar geometry. To prepare the FEMs of listric faults, the curved listric geometries are transformed into shell objects through a Python-driven 3D graphic code, Rhino 5 (see Data and Resources). This code creates numerical entities of 3D faults by preserving the spatially variable fault dip and location for the assembly of the hypothetic structural discontinuities. Each shell object of a sampled fault configuration is then inserted into the heterogeneous FEM domain to simulate the 3D earthquake rupture, after which the domain is meshed and configured with aforementioned boundary conditions accordingly.

Nonlinear Analysis by Monte Carlo Simulated Annealing

We perform a series of nonlinear analysis to invert the InSAR data for the best-fitting fault geometries of the AE, assuming a uniform slip distribution. Seven fault parameters, including fault dip δ, strike ϕ, length L, width W, and fault-center location [x_c, y_c, z_c], are used to designate the geometry and location of a planar fault. As a result, the planar and listric geometries are altogether configured by seven and six parameters, respectively. The nonlinear analysis is guided in a Bayesian manner that searches through a few thousands of fault models to minimize the error misfit $\chi^2 = e^{\mathrm{T}}\mathbf{C}^{-1}e$, in which $e = d - d_{\text{pre}}$, d and d_{pre} are, respectively, the observed and predicted LoS displacements, $\mathbf{C}$ is the covariance matrix (e.g., Huang *et al.*, 2017) and $n = 17{,}701$ is the length of the data vector. Combining simulated annealing (Jónsson *et al.*, 2002) and nested Monte Carlo method (Press, 2007), the Monte Carlo Simulated Annealing (MCSA) method searches for the fault geometry parameters that minimize χ^2. The cooling schedule of the MCSA algorithm is designed as follows:

$$T_i = T_o\left(\frac{N-i}{N}\right)^k + T_o\omega_{\min}, \tag{7}$$

$$v_{pi} = \left[\left(\frac{T_i}{T_o}\right)^{k_p} + v_{p\min}\right]v_{\text{bounded_range}}, \tag{8}$$

in which T_o and T_i are the temperature of initial step and ith step $(0, 1, 2, \ldots, N-1)$, respectively; $\omega_{\min}$ is the scaling factor of minimum temperature $T_{\min} \approx \omega_{\min}T_o$, N is the number of iteration (step); V_{pi} is the pth parameter's search range in the ith step; $V_{p\min}$ and $V_{\text{bounded_range}}$ are the last-step scaling factor and the bounded parameter range of the pth parameter, respectively; k and k_p are, respectively, the cooling/decaying coefficient of temperature and the search range of the pth parameter. The cooling schedule T_i is an array of decreasing number/temperature regulating the search of the parameter at each step, as well as the precision of the final solution. More abruptly changing (larger k and k_p) schedules refine the search range more rapidly and thus enable the solutions to converge more quickly. The distinctive advantage of MCSA over other Bayesian approaches, such as Markov chain Monte Carlo analysis (MCMC), is its effectiveness of searching for the global minimum over the local minima of the model misfit. Its resistance to local minima is reinforced by acceptance criteria

$$\chi_i^2 < \chi_{i-1}^2, \tag{9}$$

$$e^{-(\chi_i^2-\chi_{i-1}^2)\tau/T_i} > r, \tag{10}$$

in which χ_i^2 and χ_{i-1}^2 are the mean error misfit of the ith step and $(i-1)$th step, respectively; r is a random parameter between 0 and 1; and τ is a normalization factor. The criterion in equation (9) always accepts a better solution of the subsequent step, whereas the criterion in equation (10) accepts a worse solution at a certain probability, based on the misfit discrepancy $\chi_i^2 - \chi_{i-1}^2$ between the subsequent steps. The design of the cooling schedule T_i is started with an MCMC analysis that does not include the acceptance criteria. Then, we adjust the acceptance criteria and the cooling schedule in a retrospective manner and repeatedly execute the algorithm until a consistent solution is achieved. As a result, the values of T_i and τ are fixed, so that the initial

few steps of the MCSA analysis are able to escape the local minima and achieve a desired precision of the final solution.

In this study, the cooling schedule includes a total of $N = 10$ steps that individually consist of $nr = 400$–800 random realizations of the FEM-based Green's function matrix derived within a heterogeneous crustal domain. In other words, each step is slightly better than a binary systematic search (nr_{planar}: $800 \approx 7^{3.435}$, nr_{listric}: $400 \approx 6^{3.34}$) within a parametric space of 6–7 degrees of freedom. By the end of the analysis (the 10th step), the parameters will converge with a resolution equivalent to ~0.1% of their initial search ranges. τ is set to be 10^7 throughout the analysis. As such, the planar and listric geometry are optimized by selecting the solution of the lowest data-model misfit. The detailed configurations of the MCSA algorithm are described in Table 2.

Table 2
Cooling Schedule Configurations of the Monte Carlo Simulated Annealing (MCSA) Nonlinear Analyses

Parameters	Planar	Listric
N	10	10
T_o	10^6	10^6
K	3.5	3.5
$\omega_{\min}$	10^{-16}	10^{-16}
τ	10^7	10^7
DOF	7	6
Nr	800	400

DOF, degree of freedom.

Linear Inverse Analysis

After fixing the planar/listric geometry and fault location by the nonlinear analysis, we resolve the corresponding detailed slip distributions. The Green's function matrix $\mathbf{G}$ is constructed from numerous forward models of subfault, unit-sinistral, and unit-normal slip. The predicted surface displacements are then linearly interpolated from the FEM nodal positions and projected into the corresponding LoS directions of the ith InSAR image to characterize the matrix elements of $\mathbf{G}$. The coseismic slip distribution $\begin{bmatrix} m_{\text{dip}} \\ m_{\text{strike}} \end{bmatrix}$ and the plane-shift vectors P_i are inferred by linearly inverting the LoS displacements of the four InSAR images, namely, $d_{\text{S1_ASC}}$, $d_{\text{S1_DES}}$, $d_{\text{ALOS2_ASC}}$, and $d_{\text{ALOS2_DES}}$ through

$$\begin{bmatrix} m_{\text{dip}} \\ m_{\text{strike}} \\ p_{\text{S1_ASC}} \\ p_{\text{S1_DES}} \\ p_{\text{ALOS2_ASC}} \\ p_{\text{ALOS2_DES}} \end{bmatrix} = (\mathbf{G}^T\mathbf{C}^{-1}\mathbf{G})^{-1}\mathbf{G}^T\mathbf{C}^{-1}d, \tag{11}$$

in which

$$\mathbf{G} = \begin{bmatrix} \mathbf{G}_{\text{S1_ASC}} & x_{\text{S1_ASC}} & y_{\text{S1_ASC}} & 1 & 0 & 0 & 0 & 0 & 0 & 0 & 0 & 0 & 0 \\ \mathbf{G}_{\text{S1_DES}} & 0 & 0 & 0 & x_{\text{S1_DES}} & y_{\text{S1_DES}} & 1 & 0 & 0 & 0 & 0 & 0 & 0 \\ \mathbf{G}_{\text{ALOS2_ASC}} & 0 & 0 & 0 & 0 & 0 & 0 & x_{\text{ALOS2_ASC}} & y_{\text{ALOS2_ASC}} & 1 & 0 & 0 & 0 \\ \mathbf{G}_{\text{ALOS2_DES}} & 0 & 0 & 0 & 0 & 0 & 0 & 0 & 0 & 0 & x_{\text{ALOS2_DES}} & y_{\text{ALOS2_DES}} & 1 \\ \beta L & 0 & 0 & 0 & 0 & 0 & 0 & 0 & 0 & 0 & 0 & 0 & 0 \end{bmatrix} \tag{12}$$

and

$$d = \begin{bmatrix} d_{\text{S1_ASC}} \\ d_{\text{S1_DES}} \\ d_{\text{ALOS2_ASC}} \\ d_{\text{ALOS2_DES}} \end{bmatrix}, \tag{13}$$

in which $\mathbf{C}$ is the covariance matrix constructed according to Huang *et al.* (2017); the m_{dip} and m_{strike} are the dip- and strike-slip component of the subfault nodes, respectively. The plane-shift vectors $\mathbf{P}_i = [p_1, p_2, p_3]$ contain the plane-shift parameters to account for the mismodeled orbital effects inherited in the interferograms (Massonnet and Feigl, 1998; Masterlark *et al.*, 2012); x_i and y_i are the pixel locations of the data points, and 1 is a column vector of unity; β is the smoothing coefficient; and L is the second-order regularization smoothing matrix over the fault. For this event, Neumann boundary conditions are imposed ($\partial^2 s/\partial^2 x = 0$, in which x is orthogonal to the boundary) along all edges of the fault. Nonnegativity constraints are applied to the dip-slip components, whereas both right- and left-lateral strike slipping are allowed on the contrary to the fixed fault rake adopted by Lavecchia, Castaldo, *et al.* (2016) and Huang *et al.* (2017).

Results

We implement a two-step modeling approach to compare the approximation of planar fault and listric fault associated with the earthquake source of the AE: a nonlinear inversion to first estimate the optimal geometry parameters of each approximation and then a linear inversion to derive the corresponding slip distribution. The resolved slip distributions and the residuals can then provide implications on the eligibility of each geometry in simulating the AE rupture. Furthermore, we test the solution sensitivity toward the 3D crustal heterogeneity by implementing the analysis within heterogeneous (HET) domains versus homogeneous (HOM) domains. The HOM domain refers to a homogeneous isotropic elastic half-space (Okada, 1985), whereas the HET domain refers to the heterogeneous FEM domain (Fig. 2 and Table 1).

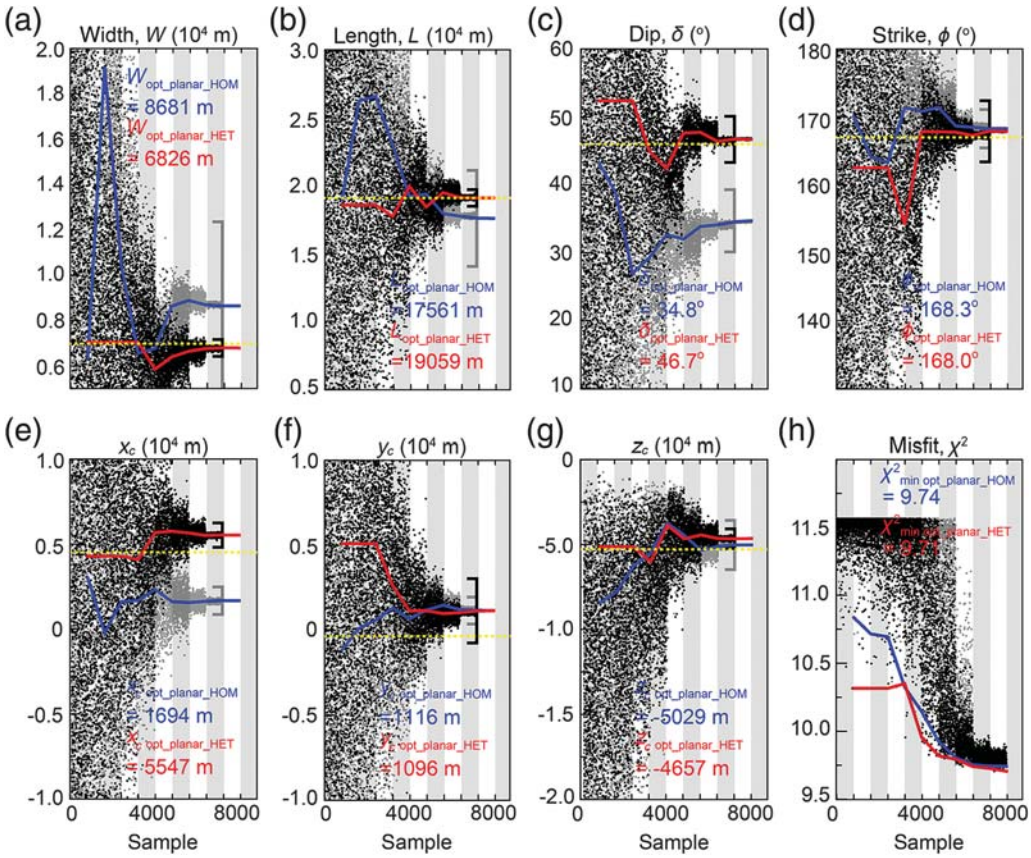

Figure 4. Solution convergence of resolving a planar source geometry in homogeneous (HOM) and heterogeneous (HET). The configurations of a planar dislocation specified by (a) width, (b) length, (c) dip, (d) strike, and (e–g) the location of fault center $[x_c, y_c, z_c]$ are optimized by minimizing (h) the model misfit χ^2 between the predicted and observed LoS displacements. Solution convergence is achieved over 10 scheduled steps/adaptions (alternating white and gray bars), each containing 800 samples. A total of 8000 planar fault geometries are sampled. The samples over HOM and HET are denoted as gray and black dots, respectively, whereas the blue (HOM) and red (HET) lines show the corresponding best solution at each adaption. The 1-sigma range of each parameter is bounded by the gray and black brackets for HOM and HET, respectively. The HET solution is found more compatible with the fault model (yellow dashed line) as suggested by Huang *et al.* (2017).

Source Model of a Uniformly Dipping Fault

Homogeneous Domain. The planar fault geometry is optimized through an MCSA-directed nonlinear analysis against the InSAR data. By searching through ~8000 elastic models in an HOM half-space, the results suggest that the coseismic deformation is predominately favored by a low-angled ($\delta_{\text{opt_planar_HOM}} = 34.8°$) SE-trending ($\phi_{\text{opt_planar_HOM}} = 168.3°$) rupture of normal slip centered at ~5 km depth and located 1694 m east and 1116 m north of 13.176° E, 42.707° N (Figs. 4 and 5). This uniformly dipping fault of 8.7 km in width and 17.6 km in length implies that the AE may have ruptured the southern section of the VF and the northern section of the GF (Fig. 4a,b). We extend the fault dimension by two times and compute the slip distribution (Fig. 6b). This configuration is comparable with what is implied in Huang *et al.* (2017) but with a slightly larger width and smaller length (Fig. 6c). A model of $\beta = 10^{-4}$ near the knee of the misfit-smoothness L curve, so that (Fig. 6a) a mean slip of 0.14 m infers a seismic moment of 2.5×10^{18} N·m, is equivalent to M_w 6.2 (Fig. 6b). Two slip asperities are located, respectively, along the VF and the GF at 1–4 km depth beneath the two heavily subsiding lobes on the surface where most of the aftershock epicenters are clustered (Fig. 6c). More slip is estimated in the latter asperity than in the former (Fig. 6b). The results indicate minor sinistral strike slip compiled with major normal faulting in proximity to the hypocenter, which is coherent with the focal plane mechanism (USGS, 2016). However, there are some systematic patterns of residuals found for both the ascending and descending InSAR data (Fig. 6d,f,h,j). For the predictions of the ascending InSAR observations (Fig. 6c,g), symmetric uplifting and subsiding signals (up to 0.1 m) are not recovered in the hanging block and foot block, respectively (Fig. 6d,h), whereas similar (but reversed) features of residuals (Fig. 6f,j) are found in the descending observations (Fig. 6e,i). Because the contribution of atmospheric noise and other orbital errors could be ruled out because of the different SAR observation dates, the nonrandom patterns of residuals may be related to the incompatibility between the model configuration and the actual rupture.

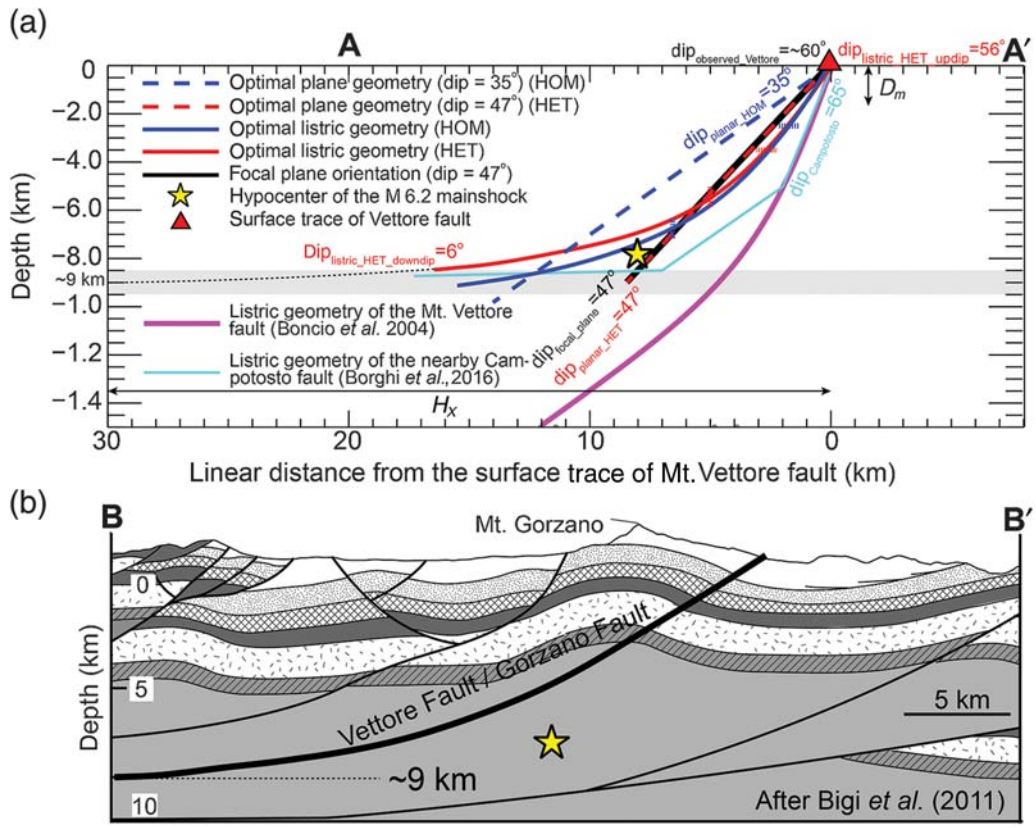

Figure 5. Nonlinearly resolved planar and listric fault and documented fault locations. (a) A cross-sectional view of the resolved planar (dashed lines) and listric (solid lines) geometries along a perpendicular profile (AA′) across the fault section (Fig. 1). The corresponding HOM and HET solutions are denoted in blue and red, respectively. The dashed lines encapsulate the optimized listric geometries before extension. The focal plane solution infers a fault dip of ~47° (thick black line). The documented listric geometry of the Vettore fault (magenta line; Boncio *et al.*, 2004) and the nearby Campotosto fault (cyan line; Borghi *et al.*, 2016) are also plotted for comparisons. The gray zone denotes the depth (~9 km) of documented decollements (Bigi *et al.*, 2009, 2011). The yellow star represents the hypocenter residing at 8 km depth. (b) A geological section (BB′ shown in Fig. 1) interpreted from local seismic tomographic profiles (Bigi *et al.*, 2011).

Heterogeneous Domain. The analysis of planar source is also performed in an HET domain constrained by a regional velocity model (Cirella *et al.*, 2012). This approach is very similar to the work of Huang *et al.* (2017) who invert the source geometry within a similar domain. A general consistency is achieved between our HET solution and that by Huang *et al.* (2017), confirming the validity of our modeling approach to resolve the source geometry (Fig. 4). After extending the HET-derived geometry by a factor of 2, both solutions show very similar surface-breaking fault geometries and locations, with comparable strikes of 167°–168°, width of 13–14 km, length of ~38 km, and a center at ~5 km depth (Fig. 7b,c). The inverted location of surface traces (Fig. 7c) is coherent with those observed in the field (Pucci *et al.*, 2017). However, this optimal fault geometry is distinctively different from that resolved in HOM (Fig. 6b), especially regarding the dip of the rupturing fault (Fig. 5a). The HET solution reveals a high-angled ($\delta_{\text{opt_planar_HET}} = 46.7°$) planar source for the AE, which is ~12° steeper than that of the HOM solution, $\delta_{\text{opt_planar_HOM}} = 34.8°$. This underlines the sensitivity of optimized source geometry toward the distribution of materials in the modeling domain, echoing the previous geodetic analyses conducted in a heterogeneous crust (compare to Hearn and Bürgmann, 2005; Trasatti *et al.*, 2011; Williams and Wallace, 2015). The corresponding slip distribution shows a majority of normal slip (up to 1 m) concentrated at 3–8 km depth beneath the subsiding regions (Fig. 7b). Contrary to the HOM solution, more slip (up to 1 m) is distributed in the asperity along the VF section than along the GF section (Fig. 7b). The majority of slip is distributed ~2–3 km deeper than that of the HOM solution (Figs. 6b and 7b). This can be explained by the steeper fault ($\delta_{\text{opt_planar_HET}} = 46.7°$ vs. $\delta_{\text{opt_planar_HOM}} = 34.8°$) of the HET solution trying to recover the deformation signals through stretching the slip horizontally and vertically (Fig. 7c,e,g,i). Additionally, the HET planar solution clearly maps the zones of positive LoS displacement above the foot block (Fig. 7e,i) and near the down-dip side of the hanging block (Fig. 7c,g), which cannot be well recovered by the HOM solution (Fig. 6c,e,g,i). Thus, the HET model better predicts the long-wavelength deformation features of InSAR signals, in the sense that the large-scale residuals become less systematic (Fig. 7d,f,h,j) than those by the HOM model (Fig. 6d,f,h,j). This yields a smaller $\chi^2 = 8.99$ of the HET solution than that of the HOM solution $\chi^2 = 9.32$.

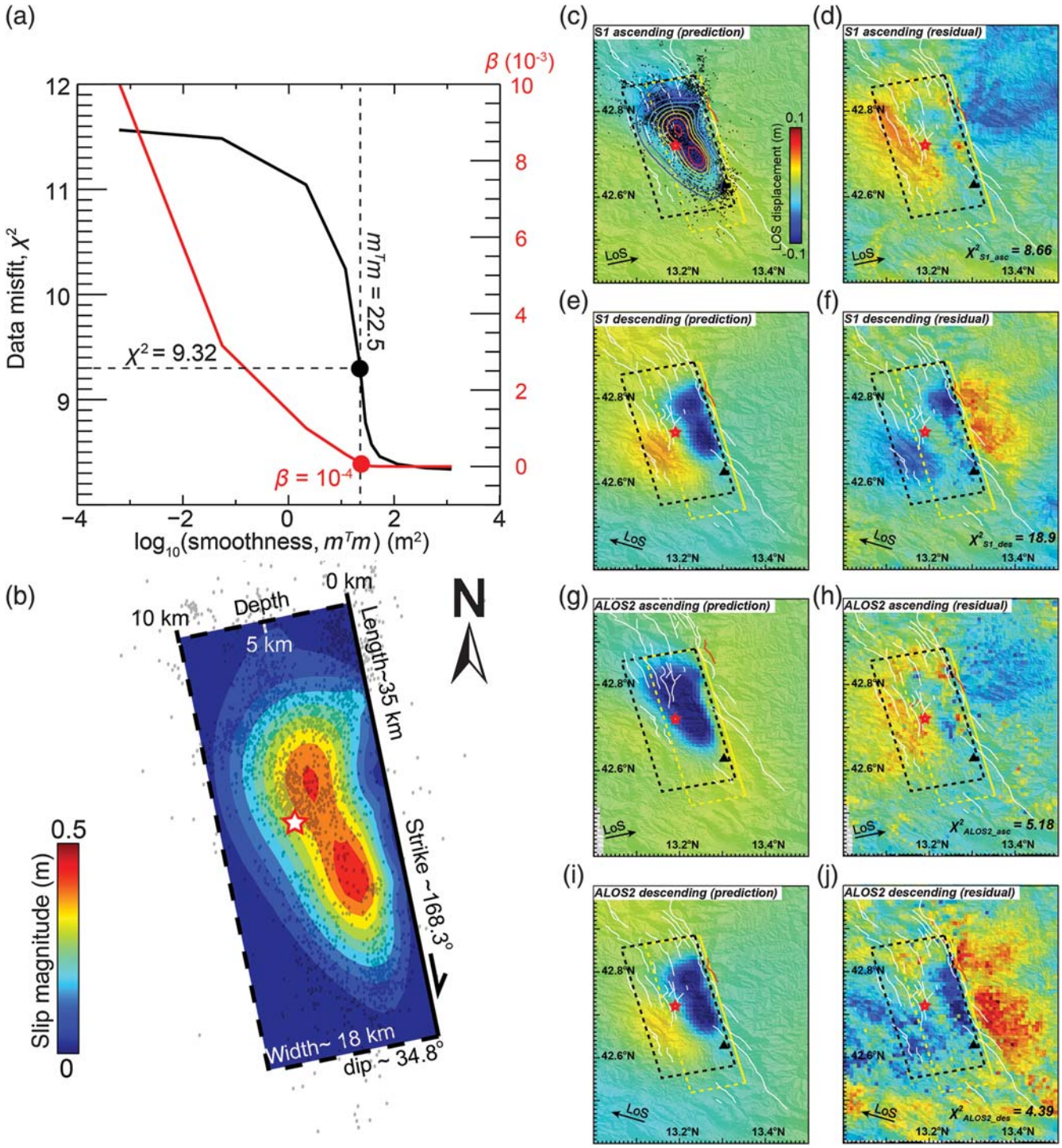

Figure 6. Slip distribution over a planar fault in HOM. (a) Trade-off curve between misfit and solution smoothness. (b) Map view of slip distribution. The gray dots are the aftershock epicenters. (c,e,g,i) Modeled and (d,f,h,j) residual LoS displacements. (d,f,h,j) The small numbers at the bottom right corner show the mean misfit of each Synthetic Aperture Radar (SAR) dataset. The black dashed line represents the fault geometry being studied. The yellow dashed line represents the geometry resolved by Huang *et al.* (2017).

Source Model of a Listric Fault

Homogeneous Domain. To further explore the down-dip curvature (if it exists) of the inverted rectangular source, we employ the arc-tangent function to constrain the listric geometry in depth. Another series of nonlinear analysis of InSAR data is conducted to estimate a uniformly slipping listric dislocation. The blind listric fault geometry is optimized over 4000 listric models to obtain a set of six parameters $[a,\ b,\ D_m,\ H_x,\ L,\ d_L]$ which best describe the earthquake-induced surface displacements (Fig. 8). Within

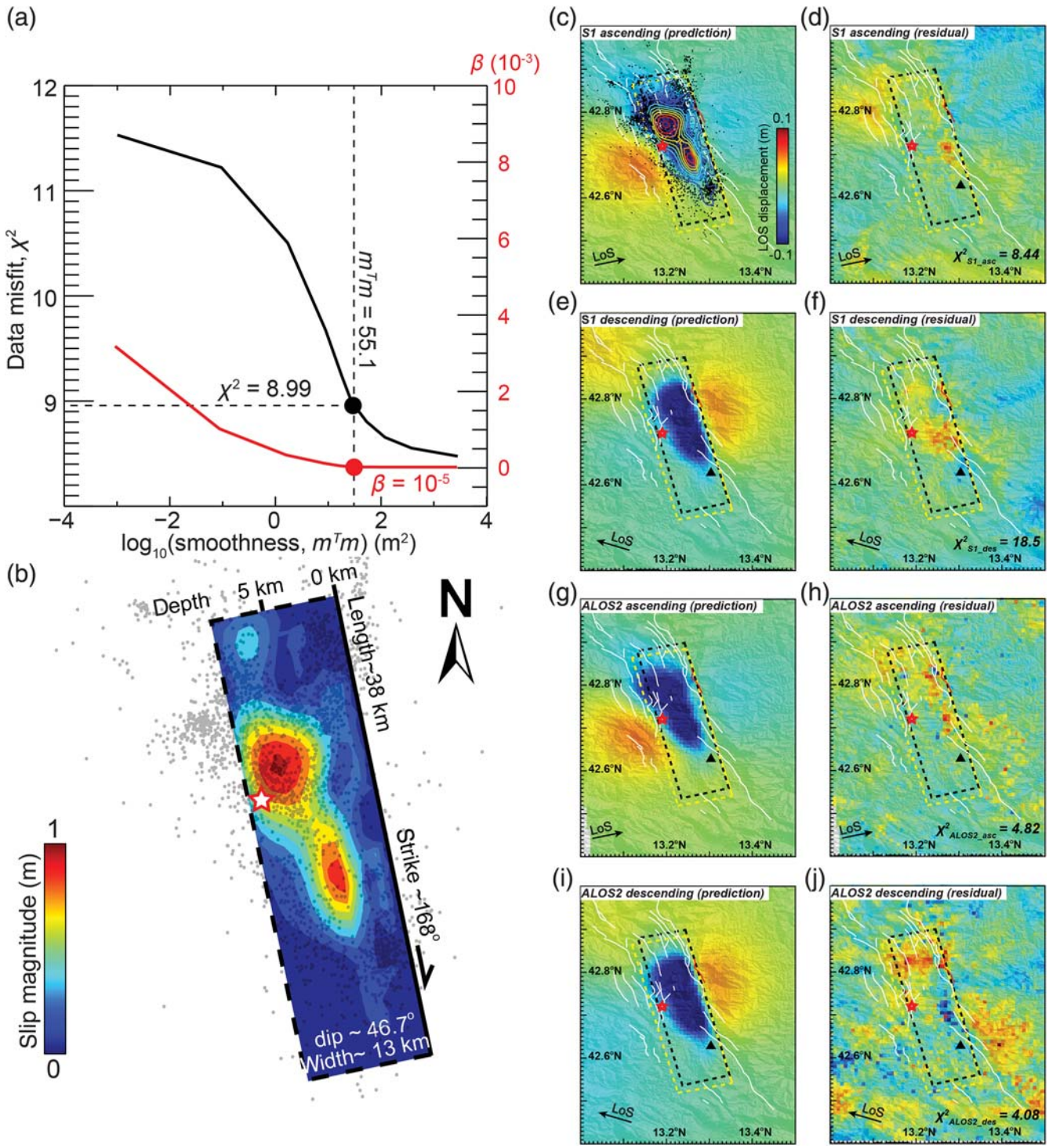

Figure 7. Slip distribution over a planar fault in HET. (a) Trade-off curve between misfit and solution smoothness. (b) Map view of slip distribution. The gray dots are the aftershock epicenters. (c,e,g,i) Modeled and (d,f,h,j) residual LoS displacements. (d,f,h,j) The small numbers at the bottom left corner show the mean misfit of each SAR dataset. The black dashed line represents the fault geometry being studied. The yellow dashed line represents the geometry resolved by Huang *et al.* (2017).

the uniform crust material, a west-dipping ($15° < \delta_{\text{listric_HOM}} < 54°$, mean = 34.5°) listric fault of $a = 11.3$ and $b = 4.7$ best fits the LoS displacements (Figs. 5a and 8). The fault is stretched horizontally by $H_x = 7.6$ km from the trace, with its center located ($x_c = 79.2$ m with respect to 42.732° N, 13.283° E) and shares a similar length ($L = 17.2$ km in Fig. 8e) with the optimized planar fault approximation ($L = 17.6$ km in Fig. 4b). Penetrating the hypocenter of the AE (42.723° N, 13.188° E) at 8 km depth (Fig. 5a), the buried uniform slip does not reach the surface

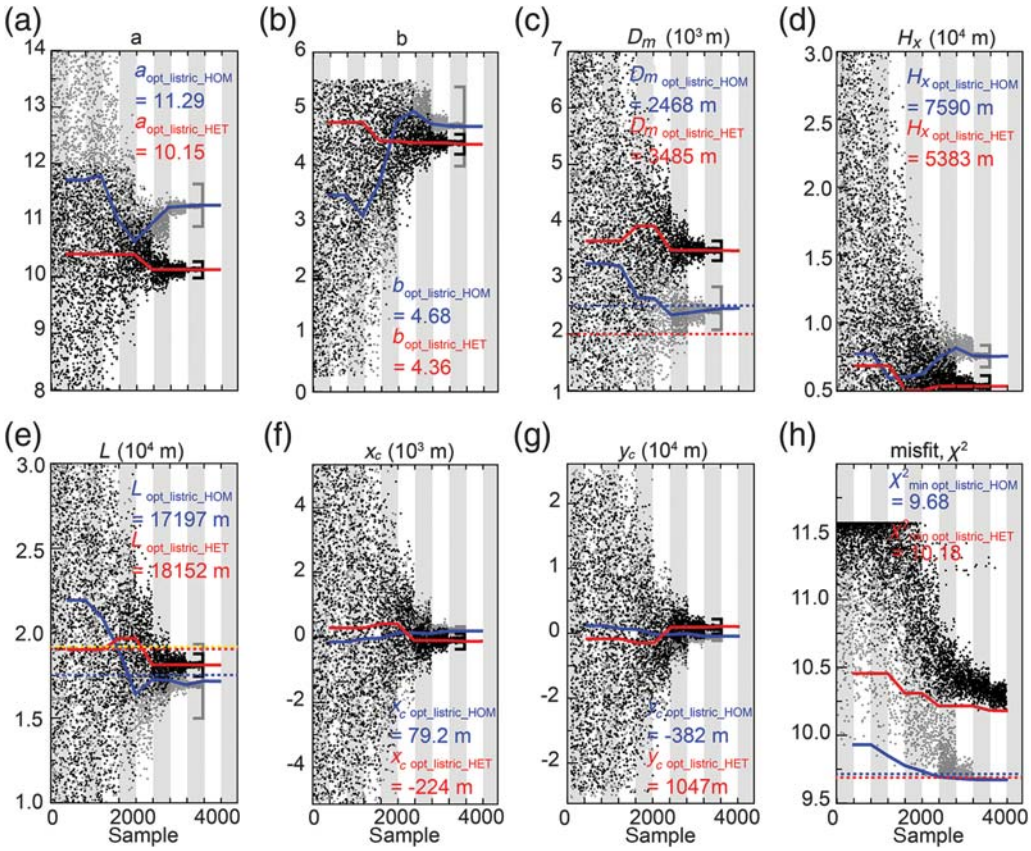

Figure 8. Solution convergence for resolving a listric source geometry in HOM and HET. The configurations of a planar dislocation specified by the arc-tangent parameter (a) a, (b) b, (c) D_m, (d) H_x, (e) L, and (f,g) the location of fault-up-dip center $[x_c, y_c]$ are optimized by minimizing (h) the data misfit χ^2 between predicted and observed LoS displacements. Solution convergence is achieved over 10 scheduled steps/adaptions (alternating white and gray bars), each with 400 samples. A total of 4000 planar fault geometries are sampled. The samples over HOM and HET are denoted as gray and black dots, respectively, whereas the blue (HOM) and red (HET) solid lines show the corresponding best solution at each adaption. The 1-sigma range of each parameter is bounded by the gray and black bracket for HOM and HET, respectively. The blue and red dashed lines represent the geometric configurations of the planar source resolved in HOM and HET, respectively. (e) The HET solution is found more compatible with the fault model (yellow dashed line) suggested by Huang *et al.* (2017).

but is terminated below a locking depth, $D_m = 2.5$ km (Fig. 8c), comparable with those ($D_{m\text{planar_HOM}} = 2.5$ km, $D_{m\text{planar_HET}} = 2.2$ km) of the HOM/HET planar solutions and other published models (Lavecchia, Castaldo, *et al.*, 2016; Huang *et al.*, 2017). For the estimated slip distribution, the fault width is extended, such that its fault dip is decreased from 61° near the surface to < 10° at 9.6 km depth (Figs. 5a and 9b). The results show that most coseismic listric rupture is concentrated at 2–8 km depth, which is deeper than the planar slip (concentrated at 1–4 km depth) in HOM (Fig. 6b). This can be explained by the generally larger depth (by ~2 km) of the listric fault than the HOM-resolved plane (Fig. 5a). We select a representative listric model with $\beta = 3.2 \times 10^{-5}$ and a mean slip of 0.17 m. Two high-slip zones are located on the VF and GF, with slightly more slip inferred on the latter and the hypocenter residing on the former, which is very similar to the interpretation of the planar HOM solution (Fig. 6b). However, a considerably larger misfit, $\chi^2 = 9.73$, is predicted by this listric HOM solution than that by the planar HOM solution, leaving discernable small-wavelength residuals over the epicentral area (Fig. 9d,f,h,j).

Heterogeneous Domain Rewrite. An optimal listric fault of $a = 10.15$ and $b = 4.4$ is obtained in the HET domain (Figs. 8 and 10). The fault is bounded beneath 3.5 km and spans over $H_x = 5.4$ km from the trace, with its center located ($x_c = 224$ m with respect to 42.727° N, 13.300° E) (Fig. 8). Its length is 18.2 km (Fig. 8e), which is comparable with those of the optimized planar sources ($L = 18$–19 km in Fig. 4b). The fault dip ranges between 8° and 48° with mean = 24.5° (Fig. 10), which is smaller than that of the listric HOM solution (Fig. 5a). On one hand, the pre-extended listric section (encapsulated by red dashed lines in Fig. 5a) of the HET solution does not attain much curvature and is visually compatible with the HET planar geometry in terms of dip and depth. On the other hand, this listric geometry is found very similar to that of the listric HOM solution, except that the down-dip side of the fault is slightly shallower (by ~1 km; Fig. 5a). This curved geometry is extended for resolving a more detailed slip distribution, with its fault dip decreasing from 56° near the surface to ~6° at 8.5 km depth (Fig. 5a). The representative model is selected at $\beta = 10^{-4}$ along the L curve (Fig. 11a). A mean slip of 0.13 m indicates

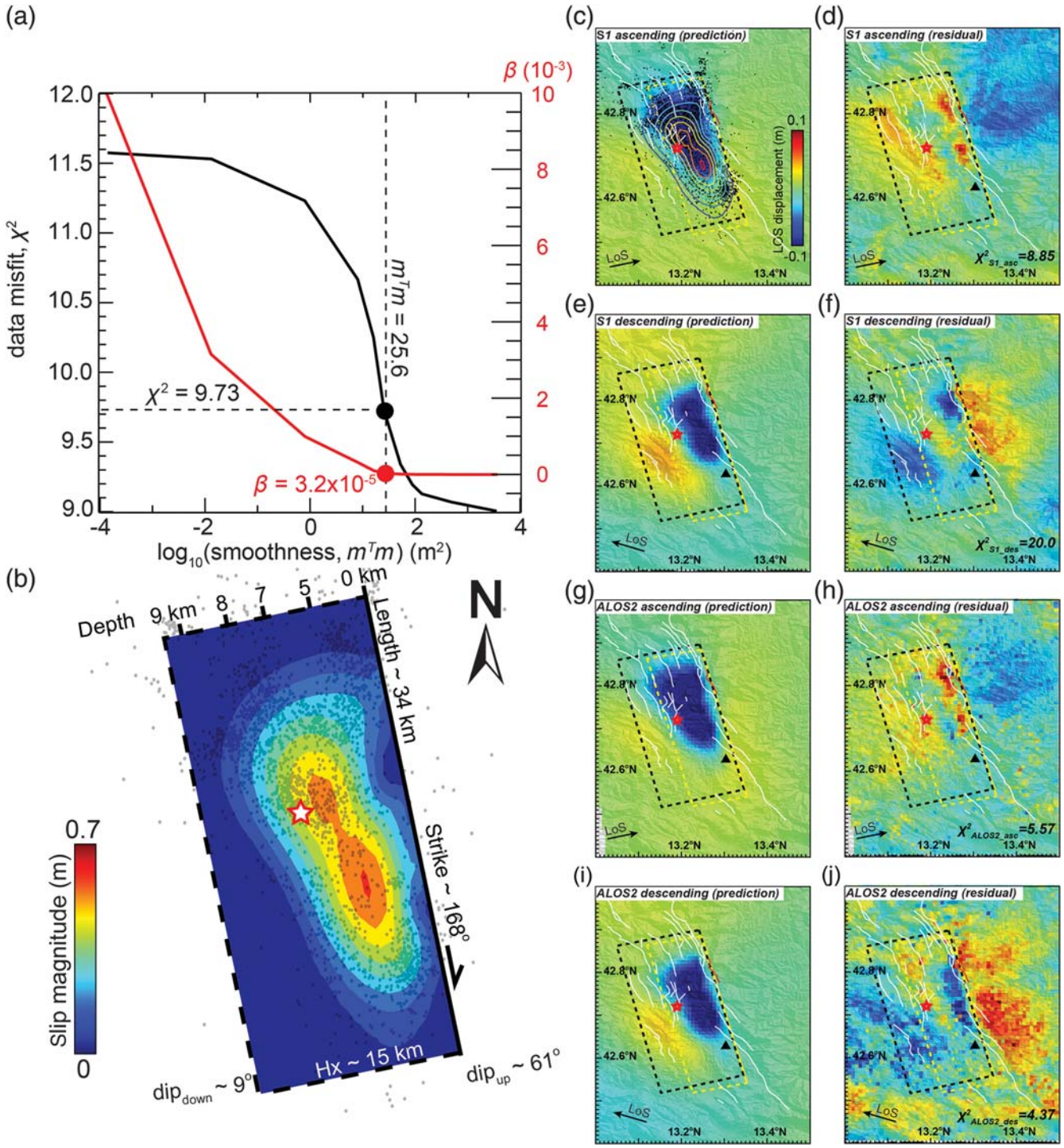

Figure 9. Slip distribution over a listric fault in HOM. (a) Trade-off curve between misfit and solution smoothness. (b) Map view of slip distribution. The gray dots are the aftershock epicenters. (c,e,g,i) Modeled and (d,f,h,j) residual LoS displacements. (d,f,h,j) The small numbers at the bottom left corner show the mean misfit of each SAR dataset. The black dashed line represents the fault geometry being studied. The yellow dashed line represents the geometry resolved by Huang *et al.* (2017).

a seismic moment of 2.87×10^{18} N·m, equivalent to M_w 6.27 (Fig. 11b). Most slip (up to 0.4 m) is modeled at 5–8 km depth near the knee of the listric curvature (Figs. 11b and 12b). A large asperity is modeled near the hypocenter, whereas a small slipping zone is estimated near the northern edge of the fault (Figs. 11b and 12b). This resolved slip model does not provide a satisfactory recovery of the observed surface deformation (Fig. 11c–f), yielding a misfit as high as 10.19 (Fig. 11a). Those localized residuals found near the surface fault trace suggest a fundamental incompatibility

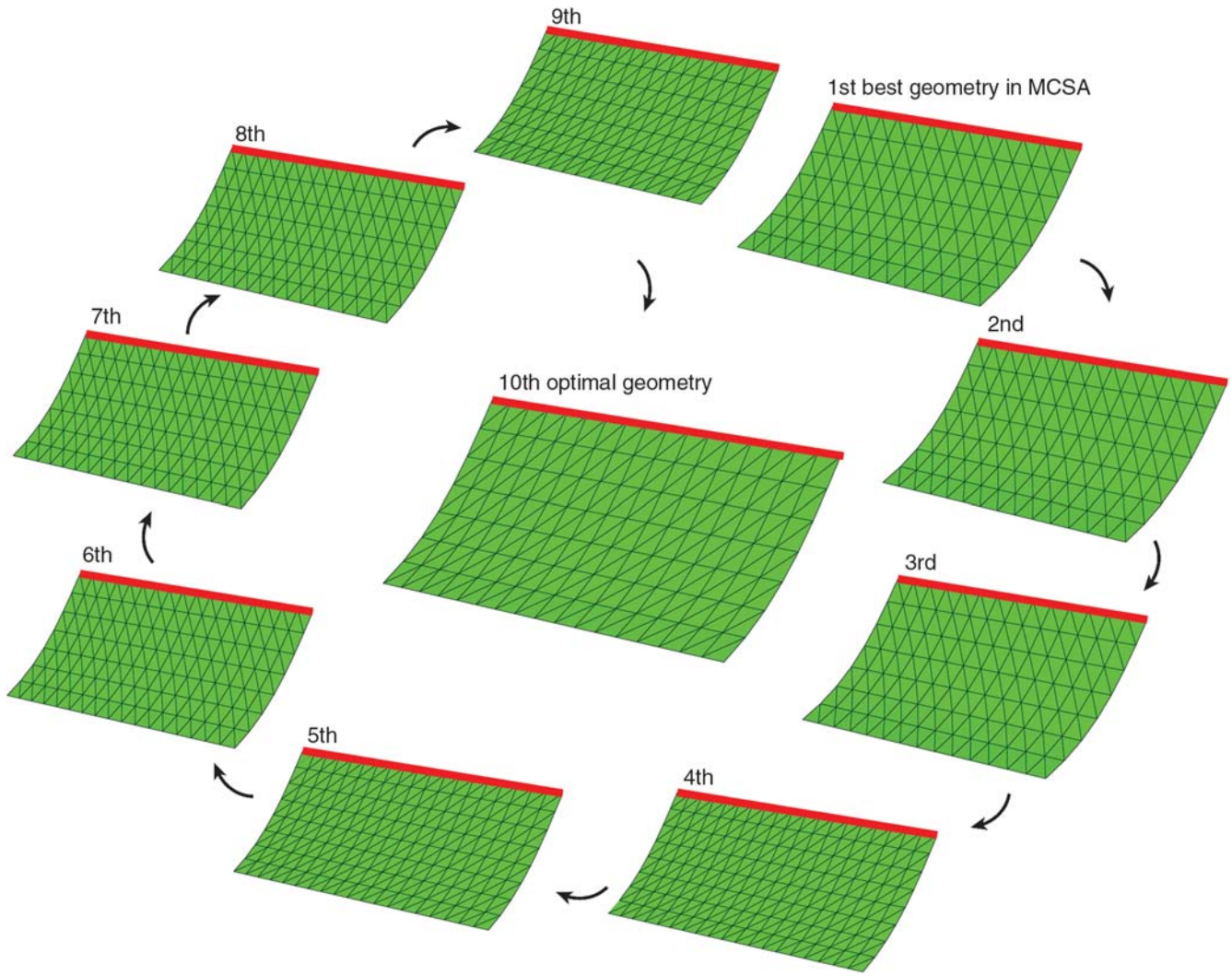

Figure 10. Resolved FEM-based listric geometry in HET through Monte Carlo Simulated Annealing (MCSA) iterations. The listric geometry is optimized with the InSAR data through the MCSA-guided nonlinear analysis. The best geometry of each iteration is updated sequentially to achieve the final optimal geometry after all 10 iterations. In HET, the meshes over the listric faults reflect the actual on-fault element configuration of FEMs.

between this listric model (especially near the fault up-dip) and the actual earthquake rupture during the AE (Fig. 11g–j).

Discussion

We investigate the earthquake source of the 2016 AE by performing nonlinear and linear inverse analyses of the InSAR data. Testing the geometry against a planar fault and a listric fault along the VF and GF, our study demonstrates an innovational approach to constrain these fault geometries and justify whether a rectangular source is sufficient for describing the deformation signature of the AE. In general, the solutions are sensitive to the distribution of material properties within the modeling domain (Figs. 4 and 8). Four types of source geometry solutions, namely planar HOM, planar HET, listric HOM, and listric HET, are obtained. The slip distribution and predicted InSAR signals of each solution are compared with the F-ratio described as

$$F = \frac{\chi_a^2}{\chi_b^2}, \tag{14}$$

in which χ_a^2 and χ_b^2 are the mean misfit of the solutions being compared. Both the planar HOM and planar HET solution show a fault strike ($\phi_{\text{opt_planar_HOM/HET}} \sim 168°$) consistent with the solution ($\phi_{\text{Huang}} = 167°$) by Huang *et al.* (2017) and that of the focal mechanism ($\phi_{\text{focal}} \sim 165°$). However, the fault dip inherited in the HOM solution ($\delta_{\text{opt_planar_HOM}} = 34.8°$) is much smaller than that of the HET solution ($\delta_{\text{opt_planar_HET}} = 46.7°$). The latter seems much more reasonable, as compared with the focal plane solution ($\delta_{\text{focal}} \sim 47°$). Therefore, we expect that the slip distribution over the HOM planar fault should not be able to predict the surface deformation as well as the HET planar fault. Regarding the slip models of a comparable moment magnitude as the AE, the HET model better predicts coseismic displacements than the HOM solution, such that $\chi^2_{\text{planar_HET}} = 8.99$ is smaller than

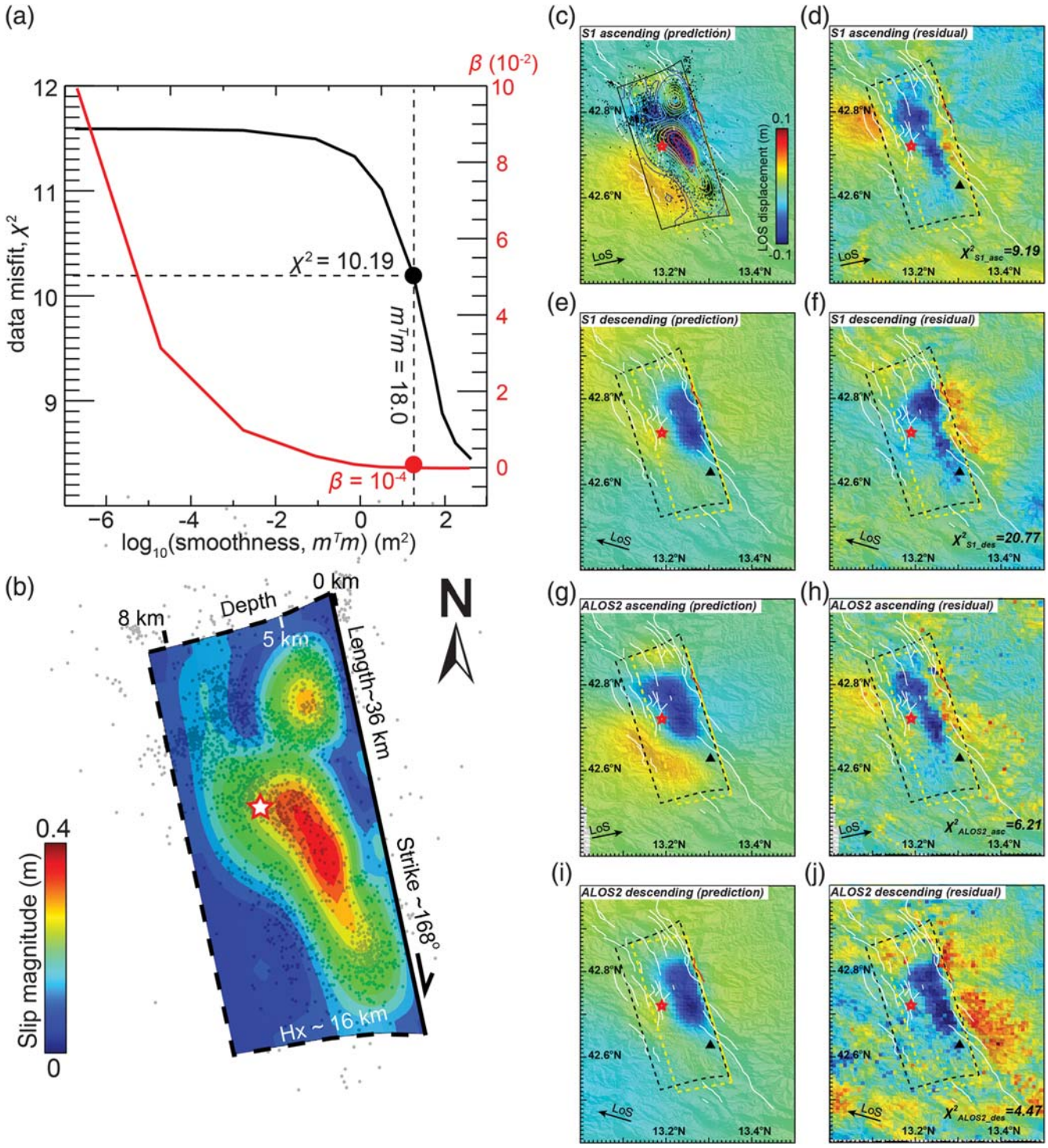

Figure 11. Slip distribution over a listric fault in HET. (a) Trade-off curve between misfit and solution smoothness. (b) Map view of slip distribution. The gray dots are the aftershock epicenters. (c,e,g,i) Modeled and (d,f,h,j) residual LoS displacements. (d,f,h,j) The small numbers at the bottom left corner show the mean misfit of each SAR dataset. The black dashed line represents the fault geometry being studied. The yellow dashed line represents the geometry resolved by Huang *et al.* (2017).

$\chi^2_{\text{planar_HOM}} = 9.32$. The value of the test statistics is $F\text{-test} = \chi^2_{\text{planar_HOM}}/\chi^2_{\text{planar_HET}} = 1.037$. Assuming a significance level of 5%, the corresponding critical value of the F-ratio is $F_{\text{critical_95\%}} = 1.031$, which is smaller than the F-test. This implies that the planar solution obtained in HOM and HET, with 95% confidence, is statistically different from each other in terms of InSAR-signal predictions and highlights a large degree of solution sensitivity toward the material domain of elastic models. The significantly worse solution of HOM could be further accounted for by the small

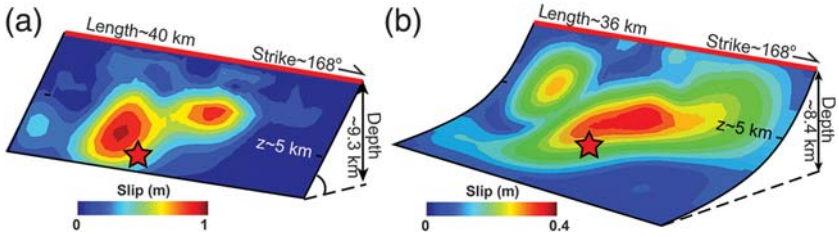

Figure 12. 3D representation of slip distributions resolved in HET. Most slip imaged along (a) the planar fault and (b) the listric fault is located at or below 5 km depth.

dip ($\delta_{\text{opt_planar_HOM}} = 34.8°$) of the planar fault estimated in a uniform half-space. As a result, most inverted slip is located in the shallower part of the crust (1–4 km depth), which does not match the hypocenter location at 8 km depth (Fig. 5a). On the contrary, the down-dip side of the HET planar fault is very close to the hypocenter (Fig. 5a), supporting that this fault configuration is a better source geometry. Meanwhile, the HET-derived fault dip ($\delta_{\text{opt_planar_HET}} = 46.7°$) is almost identical to the solution ($\delta_{\text{Huang}} = 46°$) by Huang *et al.* (2017) and that ($\delta_{\text{Lavecchia}} = 46°$) by Lavecchia, Castaldo, *et al.* (2016). The elastic dislocation theory suggests that varying fault dip influences how much fault slip is needed to reproduce the similar amount of surface deformation, for which a shallower source requires less slip than a deeper source (Okada, 1985). Both HOM and HET models can consistently image two high-slip zones along the fault but with vastly different slip magnitudes (Figs. 6b and 9b). The planar HET solution (Fig. 7b) estimates a large slip magnitude (up to 1.1 m) than the planar HOM solution (< 0.5 m; Fig. 6b). This can be explained by the smaller dip of the planar HOM fault requiring less slip to induce the similar magnitude of ground displacements. The HET model shows clearly better agreement with the estimates (< 1.2 m) of other published models (Lavecchia, Castaldo, *et al.*, 2016; Tinti *et al.*, 2016; Cheloni *et al.*, 2017; Huang *et al.*, 2017). Hence, the fault geometry and slip magnitudes computed in HET are significantly preferred over the HOM estimates. Moreover, the residuals of each solution are examined in frequency distribution plots to investigate the degree that the residuals are normally distributed (Fig. 13). The results show that the planar/listric HET solutions give a more random/symmetric distribution of residuals spatially across the epicentral region than the corresponding HOM solutions (Fig. 13a,b), because excessive amounts of negative residuals (between −0.05 and −0.03 m) are found in the HOM solutions (arrows in Fig. 13a,b). The HET solutions exhibit a narrower fluctuation of residuals ($\sigma_{\text{planar_HET}} = 0.016$ and $\sigma_{\text{listric_HET}} = 0.021$) than the corresponding HOM solutions ($\sigma_{\text{planar_HOM}} = 0.024$ and $\sigma_{\text{listric_HOM}} = 0.023$; Fig. 13a,b). This reaffirms that the inclusion of crustal material distribution in deformational models is fundamental to interpret the coseismic geodetic observations for earthquake slip and orientation (compare to Hearn and Bürgmann, 2005; Trasatti *et al.*, 2011; Williams and Wallace, 2015; Tung and Masterlark, 2016).

Furthermore, we compare the slip distributed over planar faults against listric faults to investigate if the AE has ruptured along a detachment. It is found that the up-dip geometry (above 6 km depth) of the HET-derived listric fault is fairly similar to that of the planar HET solution (Fig. 5a). The resolved listric geometry in both HOM and HET are closely corroborated with the high-angled (up to 60°) orientation of field-observed surface offsets (Fig. 1; Pucci *et al.*, 2017) and the low-angled (< 0.5°) orientation of a nearby detachment fault at a depth between 8 and 10 km (Fig. 5b; Bigi *et al.*, 2009; Borghi *et al.*, 2016). However, the corresponding slip distributions (Figs. 9b and 11b) do not provide a better fit to InSAR images than the planar fault models

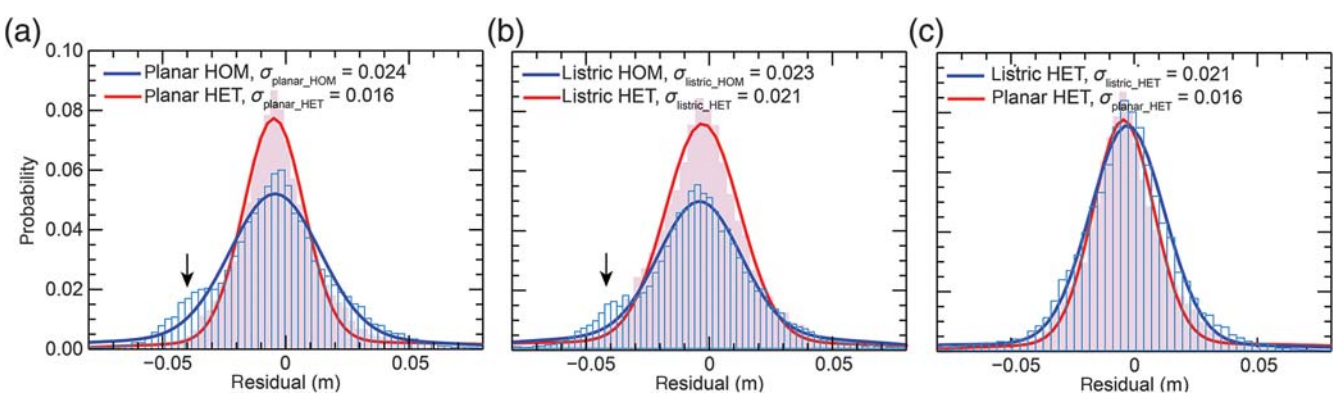

Figure 13. Residuals of the optimal models. Frequency distribution plots for the residuals of (a) the planar fault solutions and (b) the listric fault solutions. (c) The residuals of the planar solution and the listric solution in HET are further compared. σ refers to the standard deviation of the residuals. The lines refer to the best-fit Gaussian distribution of each solution. (a,b) Excessive amounts (indicated by the arrow) of overpredicted deformation (residual between −0.05 and −0.03 m) are found in the HOM solutions (blue). The HOM solutions (blue) always have a wider range of residuals than the HET solutions (light red), as reflected by their larger values of σ. (c) In HET, the planar solution attains a smaller σ of the residual distribution than the HET listric solution, though both share a similar degree of randomness, implying a better solution of the former.

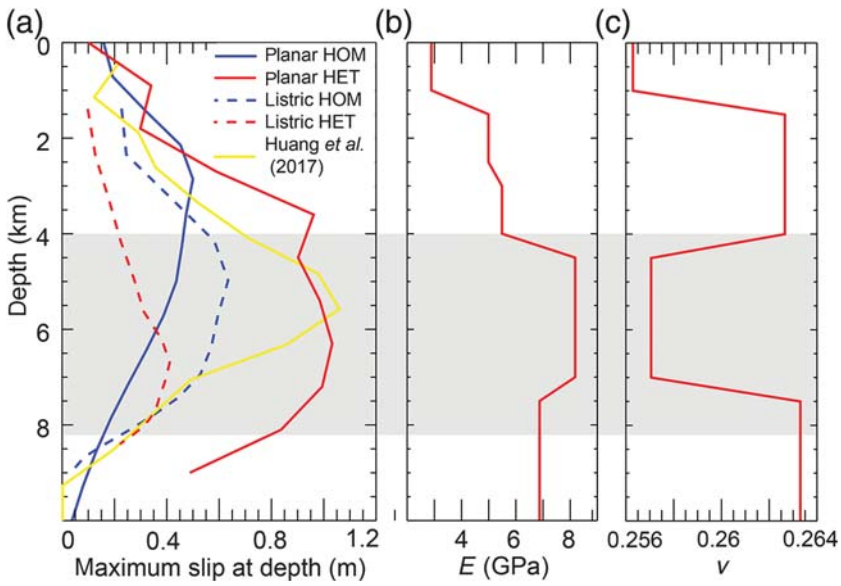

Figure 14. Comparison of resolved slip against rock properties at depth, (a) Vertical distributions of maximum slip inferred by the planar HOM, planar HET, listric HOM, and listric HET solutions are compared against that of (b) Young's modulus E and (c) Poisson's ratio v at depth. A sharp increase of rock rigidity is found at ~4 km depth, beneath which the crust is ~55% more rigid ($E \sim 85$ GPa) than that above ($E \sim 55$ GPa). The hypocenter (depth = 8 km) and most of the earthquake slip are embedded within such a layer of stronger rock (gray-shaded zone). The relation is also found in the slip model suggested by Huang *et al.* (2017).

(Figs. 6b and 7b), though the inverted locations of two high-slip asperities along the VF and GF are very similar. In HOM, the value of the test statistics is $F\text{-test} = \chi^2_{\text{listric_HOM}}/\chi^2_{\text{planar_HOM}} = 9.72/9.32 = 1.043$, which is larger than $F_{\text{critical_95\%}} = 1.031$. This suggests that the planar solution is a significantly better model than the listric solution. A similar phenomenon is also revealed in those HET solutions. Although the residuals of both the planar HET and listric HET models follow a Gaussian distribution (Fig. 13c), the listric rupture gives rise to a substantially larger $\chi^2_{\text{listric_HET}} = 10.50$ than that of the planar solution $\chi^2_{\text{planar_HET}} = 8.99$, yielding $\chi^2_{\text{listric_HET}}/\chi^2_{\text{planar_HET}} = 10.19/8.99 = 1.133$, which is also larger than $F_{\text{critical_95\%}} = 1.031$. In particular, the listric HET model seems to merge the two asperities (implied by all other models in Figs. 6, 7, and 9) along the VF and GF into a single large slip asperity (with smaller slip magnitudes) near the hypocenter (Figs. 11b and 12b), in comparison with the planar HET model (Figs. 7b and 12a). Meanwhile, a shallower dextral strike-slipping zone is modeled about 10 km north of the epicenter (Figs. 11b and 12b), which is considered as a numerical artifact of slip oscillation due to the incompatible source geometry. Though this spurious pattern could be removed by imposing an extra positivity constraint to limit the strike-slipping components in a sinistral manner (compare to Hudnut *et al.*, 1996); such an artifact does not exist in the planar HET solution with the absence of this constraint (Fig. 7b). Moreover, the slip magnitudes derived by the planar HET solution (up to 1.1 m) are vastly different from those (< 0.43 m) of the listric HET solution. The former is found significantly more consistent with other published source models of the AE (Lavecchia, Castaldo, *et al.*, 2016; Tinti *et al.*, 2016; Cheloni *et al.*, 2017; Huang *et al.*, 2017). It appears that the HET planar fault model of ~47° dip better explains the LoS displacements near the surface trace of the VF and GF (Fig. 7d–j) than the listric models (Fig. 11d–j), implying that the near-surface fault dip should be gentler than the listric estimates of ~56°. Therefore, we accept the hypothesis that a planar approximation is able to adequately describe the earthquake rupture without introducing extra down-dip listric characteristics, at a 95% confidence level. This supports the validity of the existing fault models, assuming a uniform-dipping fault for the AE (Lavecchia, Castaldo, *et al.*, 2016; Tinti *et al.*, 2016; Cheloni *et al.*, 2017; Huang *et al.*, 2017).

In our study, all derived models imply buried slip beneath 2 km depth regardless of the adopted fault geometry (Fig. 14). In general, major fault rupture is located deeper in HET models than that in HOM models, as a result of introducing spatially varying rock properties in the elastic dislocation models. This vertical distribution of slip could be related to the *in situ* lithology (Turcotte and Schubert, 2014) and the corresponding frictional behaviors (Byerlee, 1978). The relationship between the slip magnitude and subsurface rock materials is estimated along a vertical profile of the faults (Fig. 14). The majority of slip is found in a depth range between 3 and 8 km, similar to that (4 and 7 km) suggested by Huang *et al.* (2017) and that (5 and 7 km) by Lavecchia, Castaldo, *et al.* (2016). For the planar HET solution, the hypocenter (at 8 km depth) and maximum slip (~1 m at 7 km depth) are found within a rock layer of higher strength, referred to Triassic dolomites (Bigi *et al.*, 2011). Seismic velocity models suggest that there exists a lithological/transitional boundary at ~4 km depth (Cirella *et al.*, 2012), where the rock rigidity (Young's modulus E) is suddenly enhanced by more than 50%, from ~55 to 85 GPa ($\Delta E = \sim 30$ GPa), and Poisson's ratio v drops slightly. This stronger rock sublayer coincides with the majority (~97%) of aftershocks occurring between 6 and 14 km at the depth (USGS, 2016) where the active Altotiberina fault resides (Boncio *et al.*, 2004). In contrast, very limited coseismic rupture is estimated (< 0.2 m) near the surface (Fig. 14) where the weaker material is reflected by Young's modulus as low as 2 GPa. Therefore, the superposition between the high-slip asperities and high subsurface rigidity implies a possible structural control exerted on the seismic nucleation and propagation of the AE. This can be partially accounted for by the fact

that the enhanced rock stiffness encourages the tectonic stress accumulation and the release of strain energy as violent earthquakes at the incidence of frictional failure (Kaproth and Marone, 2013). The brittle upper crust (4–10 km) of the central Apennines may explain why shallow seismicities (average ~11 km) are usually detected over the past century (since 1906; USGS, 2016). Moreover, the juxtaposition of the underlying weak graben-fill sediments (0–4 km depth; Bigi *et al.*, 2003, 2009, 2011) and the shallow active fault systems near the foreland basins can lead to severe surface damages during earthquakes, which should be taken into consideration when evaluating the seismic hazard in central Italy (compare Valensise *et al.*, 2016).

Conclusions

The AE took place within a zone of the central Apennines where systems of detachment and decollement faults are well documented. Incorporated with an advanced FEM technique, our study solves for the listric fault geometries that best describe the InSAR observations of coseismic deformation, as compared with the planar fault models. As such, we test the hypothesis whether a planar fault is sufficient to describe the earthquake source of the AE. The novelty of this analysis resides in its capability of using thousands of different fault configurations to simulate a complex listric geometry within a crust of distributed rock material. FEMs of about a half-million elements are adopted to assemble the heterogeneous domain for computing the elastic dislocation. The fault geometries estimated for an HET crust are significantly different from those estimated for an HOM half-space, underlining the solution sensitivity of inverse analysis toward the material definition of the elastic-modeling domain. In particular, the HET-resolved planar slip matches the hypocenter location at 8 km depth and attains a fault dip of 47° (as also supported by Huang *et al.*, 2017), almost identical to the moment tensor solution, whereas that of the HOM solution is offset by ~14°. This suggests that a more realistic numerical domain is necessary to accurately image a physical fault geometry from the geodetic data, particularly in the area of complex tectonic settings, such as the central Apennines. For an HET domain, our results show that the prediction of surface deformation is not improved by introducing the geometric complexity of down-dip fault curvature. This suggests that a rectangular source approximation is sufficient to simulate the fault rupture of the AE, validating the current usage of such approximation to analyze the event. Moreover, the resolved slip distribution reveals that fault slip is generally located within a layer of stronger rock at between 4 and 8 km depth. This is beneath a lithological boundary at ~4 km when the shallow weaker units ($E \sim 55$ GPa) are suddenly transitioned to the stronger bedrock ($E \sim 85$ GPa). Coupled with the ongoing tectonic activities of the central Apennines, the correlation between the slip distribution of the AE and subsurface rock rigidity implies a possible structural control on the earthquake nucleation and propagation, which provides insight on assessing the seismic hazard of central Italy.

Data and Resources

Finite-element models were built in Abaqus v. 6.12 (https://www.3ds.com/products-services/simulia/products/abaqus, last accessed August 2013) and Rhino 5 (https://www.rhino3d.com, last accessed May 2015). Aftershock information is retrieved from the U.S. Geological Survey (USGS) earthquake catalog through https://earthexplorer.usgs.gov/ and https://earthquake.usgs.gov/earthquakes/eventpage/us10006g7d#executive (last accessed September 2016). A global crustal velocity model CRUST2.0 was retrieved from https://asterweb.jpl.nasa.gov/gdem.asp (last accessed September 2016). Some plots were made using the Interactive Data Language v. 8.5.1 (www.harrisgeospatial.com/ProductsServices/IDL.aspx, last accessed August 2013).

Acknowledgments

The authors are very grateful to Editor-in-Chief Thomas L. Pratt and Luis Angel and two anonymous reviewers for comments and suggestions that significantly improved the article. This material is based upon work supported by the National Science Foundation under Grant Number 1316082. This work is also supported, in part, by National Aeronautics and Space Administration (NASA) Grant Number NNX17AD96G and NASA Jet Propulsion Laboratory (JPL) Subcontract Number 1468758. Academic licensing and technical support for Abaqus software was provided by Dassault Systèmes Simulia Corp. The authors express their gratitude to Mong-Han Huang (Advanced Rapid Imaging and Analysis [ARIA]/JPL/NASA) for sharing the Sentinel 1-A/B and Advanced Land Observation Satellite (ALOS)-2 Interferometric Synthetic Aperture Radar (InSAR) data. The authors also thank Sabina Bigi for providing the figures of the near-field geological cross section and Kurt Katzenstein for his helpful criticism and comments.

References

Albano, M., S. Barba, M. Saroli, M. Moro, F. Malvarosa, M. Costantini, C. Bignami, and S. Stramondo (2015). Gravity-driven postseismic deformation following the M_w 6.3 2009 L'Aquila (Italy) earthquake, *Sci. Rep.* **5,** doi: 10.1038/srep16558.

Ameri, G., F. Gallovič, F. Pacor, and A. Emolo (2009). Uncertainties in strong ground-motion prediction with finite-fault synthetic seismograms: An application to the 1984 M 5.7 Gubbio, central Italy, earthquake, *Bull. Seismol. Soc. Am.* **99,** 647–663.

Anzidei, M., and S. Pondrelli (2016). The Amatrice seismic sequence: Preliminary data and results, *Ann. Geophys.* **59,** Fast Track 5.

Atzori, S., I. Hunstad, M. Chini, S. Salvi, C. Tolomei, C. Bignami, S. Stramondo, E. Trasatti, A. Antonioli, and E. Boschi (2009). Finite fault inversion of DInSAR coseismic displacement of the 2009 L'Aquila earthquake (central Italy), *Geophys. Res. Lett.* **36,** doi: 10.1029/2009GL039293.

Bassin, C. (2000). The current limits of resolution for surface wave tomography in North America, *Eos Trans. AGU* **81,** F897.

BBC (2016). Italy earthquake toll rises to 297 after two die of injuries, *BBC*, available at http://www.bbc.com/news/world-europe-37390893 (last accessed September 2016).

Bigi, S., P. Casero, and G. Ciotoli (2011). Seismic interpretation of the Laga basin; constraints on the structural setting and kinematics of the central Apennines, *J. Geol. Soc.* **168,** 179–190.

Bigi, S., F. Lenci, C. Doglioni, J. C. Moore, E. Carminati, and D. Scrocca (2003). Décollement depth versus accretionary prism dimension in the Apennines and the Barbados, *Tectonics* **22,** doi: 10.1029/2002TC001410.

Bigi, S., S. Milli, S. Corrado, P. Casero, L. Aldega, F. Botti, M. Moscatelli, O. Stanzione, F. Falcini, and M. Marini (2009). Stratigraphy, structural setting and burial history of the Messinian Laga basin in the context of Apennine foreland basin system, *J. Medit. Earth Sci.* **1,** 61–84.

Boncio, P., G. Lavecchia, and B. Pace (2004). Defining a model of 3D seismogenic sources for seismic hazard assessment applications: The case of central Apennines (Italy), *J. Seismol.* **8,** 407–425.

Borghi, A., A. Aoudia, F. Javed, and R. Barzaghi (2016). Precursory slow-slip loaded the 2009 L'Aquila earthquake sequence, *Geophys. J. Int.* **205,** 776–784.

Byerlee, J. (1978). Friction of rocks, *Pure Appl. Geophys.* **116,** 615–626.

Calamita, F., and A. Pizzi (1992). Tettonica quaternaria nella dorsale appenninica umbro-marchigiana e bacini intrappenninici associati, *Studi Geologici Camerti* (in Italian).

Calamita, F., and A. Pizzi (1994). Recent and active extensional tectonics in the southern Umbro-Marchean Apennines (central Italy), *Mem. Soc. Geol. Ital.* **48,** 541–548.

Chau, K. T., and J. H. Y. Lo (2001). Soil amplification in Hong Kong under far field earthquakes, in *Soft Soil Engineering*, The Hong Kong Polytechnic University, Hong Kong, China, 245.

Cheloni, D., V. De Novellis, M. Albano, A. Antonioli, M. Anzidei, S. Atzori, A. Avallone, C. Bignami, M. Bonano, and S. Calcaterra (2017). Geodetic model of the 2016 central Italy earthquake sequence inferred from InSAR and GPS data, *Geophys. Res. Lett.* **44,** 6778–6787.

Chiaraluce, L., R. Di Stefano, E. Tinti, L. Scognamiglio, M. Michele, E. Casarotti, M. Cattaneo, P. De Gori, C. Chiarabba, and G. Monachesi (2017). The 2016 central Italy seismic sequence: A first look at the mainshocks, aftershocks, and source models, *Seismol. Res. Lett.* **88,** no. 3, 757–771.

Ciaccio, M., M. Barchi, C. Chiarabba, F. Mirabella, and E. Stucchi (2005). Seismological, geological and geophysical constraints for the Gualdo Tadino fault, Umbria–Marche Apennines (central Italy), *Tectonophysics* **406,** 233–247.

Cirella, A., A. Piatanesi, M. Cocco, E. Tinti, L. Scognamiglio, A. Michelini, A. Lomax, and E. Boschi (2009). Rupture history of the 2009 L'Aquila (Italy) earthquake from non-linear joint inversion of strong motion and GPS data, *Geophys. Res. Lett.* **36,** doi: 10.1029/2009GL039795.

Cirella, A., A. Piatanesi, E. Tinti, M. Chini, and M. Cocco (2012). Complexity of the rupture process during the 2009 L'Aquila, Italy, earthquake, *Geophys. J. Int.* **190,** 607–621.

Eleonora, R., M. Walter, and B. Maurizio (2002). The edge dislocation problem in a layered elastic medium, *Geophys. J. Int.* **149,** 508–523.

Fernandez, J., T. T. Yu, and J. B. Rundle (1996). Deformation produced by a rectangular dipping fault in a viscoelastic-gravitational layered Earth model. Part 1. Thrust fault—FLTGRV and FLTGRH FORTRAN programs, *Comput. Geosci.* **22,** 735–750.

Galadini, F., and P. Galli (2003). Paleoseismology of silent faults in the central Apennines (Italy): The Mt. Vettore and Laga Mts. faults, *Ann. Geophys.* doi: 10.4401/ag-3457.

He, Y., W. Wang, and Z. Yao (2003). Static deformation due to shear and tensile faults in a layered half-space, *Bull. Seismol. Soc. Am.* **93,** 2253–2263.

Hearn, E. H., and R. Bürgmann (2005). The effect of elastic layering on inversions of GPS data for coseismic slip and resulting stress changes: Strike-slip earthquakes, *Bull. Seismol. Soc. Am.* **95,** 1637–1653.

Huang, M. H., E. J. Fielding, C. Liang, P. Milillo, D. Bekaert, D. Dreger, and J. Salzer (2017). Coseismic deformation and triggered landslides of the 2016 M_w 6.2 Amatrice earthquake in Italy, *Geophys. Res. Lett.* **44,** 1266–1274.

Hudnut, K., Z. Shen, M. Murray, S. McClusky, R. King, T. Herring, B. Hager, Y. Feng, P. Fang, and A. Donnellan (1996). Co-seismic displacements of the 1994 Northridge, California, earthquake, *Bull. Seismol. Soc. Am.* **86,** S19–S36.

Hughes, K. L. H., T. Masterlark, and W. D. Mooney (2010). Poroelastic stress-triggering of the 2005 M 8.7 Nias earthquake by the 2004 M 9.2 Sumatra–Andaman earthquake, *Earth Planet. Sci. Lett.* **293,** 289–299.

Hutton, W., C. DeMets, O. Sanchez, G. Suarez, and J. Stock (2001). Slip kinematics and dynamics during and after the 1995 October 9 M_w = 8.0 Colima–Jalisco earthquake, Mexico, from GPS geodetic constraints, *Geophys. J. Int.* **146,** 637–658.

Jónsson, S., H. Zebker, P. Segall, and F. Amelung (2002). Fault slip distribution of the 1999 M_w 7.1 Hector Mine, California, earthquake, estimated from satellite radar and GPS measurements, *Bull. Seismol. Soc. Am.* **92,** 1377–1389.

Jovanovich, D. B., M. I. Husseini, and M. A. Chinnery (1974). Elastic dislocations in a layered half-space—I. Basic theory and numerical methods, *Geophys. J. Int.* **39,** 205–217.

Kaproth, B. M., and C. Marone (2013). Slow earthquakes, preseismic velocity changes, and the origin of slow frictional stick-slip, *Science* **341,** 1229–1232.

Kyriakopoulos, C., T. Masterlark, S. Stramondo, M. Chini, and C. Bignami (2013). Coseismic slip distribution for the M_w 9 2011 Tohoku-Oki earthquake derived from 3-D FE modeling, *J. Geophys. Res.* **118,** 3837–3847.

Lavecchia, G., G. M. Adinolfi, R. de Nardis, F. Ferrarini, D. Cirillo, F. Brozzetti, R. De Matteis, G. Festa, and A. Zollo (2016). Multidisciplinary inferences on a newly recognized active east-dipping extensional system in central Italy, *Terra Nova* doi: 10.1111/ter.12251.

Lavecchia, G., R. Castaldo, R. de Nardis, V. De Novellis, F. Ferrarini, S. Pepe, F. Brozzetti, G. Solaro, D. Cirillo, M. Bonano, *et al.* (2016). Ground deformation and source geometry of the August 24, 2016 Amatrice earthquake (central Italy) investigated through analytical and numerical modeling of DInSAR measurements and structural-geological data, *Geophys. Res. Lett.* **43,** 12,389–12,398.

Li, H., A. Michelini, L. Zhu, F. Bernardi, and M. Spada (2007). Crustal velocity structure in Italy from analysis of regional seismic waveforms, *Bull. Seismol. Soc. Am.* **97,** 2024–2039.

Livio, F. A., A. Michetti, E. Vittori, L. Gregory, L. Wedmore, L. Piccardi, E. Tondi, G. Roberts, A. Blumetti, and L. Bonadeo (2016). Surface faulting during the August 24, 2016, central Italy earthquake (M_w 6.0): preliminary results, *Ann. Geophys.* **59,** doi: 10.4401/ag-7197.

Margheriti, S. M., F. Mele, G. Selvaggi, A. Basili, and E. Boschi (1998). The 1997 Umbria-Marche, Italy, earthquake sequence, *Geophys. Res. Lett.* **25,** 2861–2864.

Marzorati, S., M. Massa, M. Cattaneo, G. Monachesi, and M. Frapiccini (2014). Very detailed seismic pattern and migration inferred from the April 2010 Pietralunga (northern Italian Apennines) micro-earthquake sequence, *Tectonophysics* **610,** 91–109.

Massonnet, D., and K. L. Feigl (1998). Radar interferometry and its application to changes in the Earth's surface, *Rev. Geophys.* **36,** 441–500.

Masterlark, T. (2003). Finite element model predictions of static deformation from dislocation sources in a subduction zone: Sensitivities to homogeneous, isotropic, Poisson-solid, and half-space assumptions, *J. Geophys. Res.* **108,** 1029–2510.

Masterlark, T., and K. L. H. Hughes (2008). Next generation of deformation models for the 2004 M 9 Sumatra-Andaman earthquake, *Geophys. Res. Lett.* **35,** no. 19, 19310.

Masterlark, T., C. DeMets, H. Wang, O. Sanchez, and J. Stock (2001). Homogeneous vs heterogeneous subduction zone models: Coseismic and postseismic deformation, *Geophys. Res. Lett.* **28,** 4047–4050.

Masterlark, T., K. L. Feigl, M. Haney, J. Stone, C. Thurber, and E. Ronchin (2012). Nonlinear estimation of geometric parameters in FEMs of volcano deformation: Integrating tomography models and geodetic data for Okmok volcano, Alaska, *J. Geophys. Res.* **117,** doi: 10.1029/2011JB008811.

Michele, M., R. Di Stefano, L. Chiaraluce, M. Cattaneo, P. De Gori, G. Monachesi, D. Latorre, S. Marzorati, L. Valoroso, and C. Ladina (2016). The Amatrice 2016 seismic sequence: A preliminary look at

the mainshock and aftershocks distribution, *Ann. Geophys.* **59,** doi: 10.4401/ag-7227.

Morelli, A., and E. Boschi (1998). Moment tensor analysis of the central Italy earthquake sequence of September–October 1997, *Geophys. Res. Lett.* **25,** 1971–1974.

Nocquet, J.-M. (2012). Present-day kinematics of the Mediterranean: A comprehensive overview of GPS results, *Tectonophysics* **579,** 220–242.

Okada, Y. (1985). Surface deformation due to shear and tensile faults in a half-space, *Bull. Seismol. Soc. Am.* **75,** 1135–1154.

Pan, E. (1999). Green's functions in layered poroelastic half-spaces, *Int. J. Numer. Anal. Meth. Geomech.* **23,** 1631–1653.

Pizzi, A., F. Calamita, M. Coltorti, and P. Pieruccini (2002). Quaternary normal faults, intramontane basins and seismicity in the Umbria-Marche-Abruzzi Apennine Ridge (Italy): Contribution of neotectonic analysis to seismic hazard assessment, *Boll. Soc. Geol. Ital., Spec. Publ.* **1,** 923–929.

Press, W. H. (2007). *Numerical Recipes 3rd Edition: The Art of Scientific Computing*, Cambridge University Press, Cambridge, United Kingdom.

Pucci, S., P. De Martini, R. Civico, F. Villani, R. Nappi, T. Ricci, R. Azzaro, C. Brunori, M. Caciagli, and F. Cinti (2017). Coseismic ruptures of the 24 August 2016, M_w 6.0 Amatrice earthquake (central Italy), *Geophys. Res. Lett.* **44,** 2138–2147.

Reilinger, R., S. McClusky, P. Vernant, S. Lawrence, S. Ergintav, R. Cakmak, H. Ozener, F. Kadirov, I. Guliev, and R. Stepanyan (2006). GPS constraints on continental deformation in the Africa-Arabia-Eurasia continental collision zone and implications for the dynamics of plate interactions, *J. Geophys. Res.* **111,** doi: 10.1029/2005JB004051.

Sato, R. (1971). Crustal deformation due to dislocation in a multi-layered medium, *J. Phys. Earth* **19,** 31–46.

Savage, J. (1987). Effect of crustal layering upon dislocation modeling, *J. Geophys. Res.* **92,** 10,595–10,600.

Savage, J. (1998). Displacement field for an edge dislocation in a layered half-space, *J. Geophys. Res.* **103,** 2439–2446.

Scarfì, L., S. Imposa, R. Raffaele, and A. Scaltrito (2009). Crustal seismic velocity in the Marche region (central Italy): Computation of a minimum 1-D model with seismic station corrections, *Environ. Geol.* **56,** 1115–1121.

Scognamiglio, L., E. Tinti, and M. Quintiliani (2016). The first month of the 2016 central Italy seismic sequence: fast determination of time domain moment tensors and finite fault model analysis of the M_L 5.4 aftershock, *Ann. Geophys.* **59,** doi: 10.4401/ag-7246.

Serpelloni, E., G. Vannucci, S. Pondrelli, A. Argnani, G. Casula, M. Anzidei, P. Baldi, and P. Gasperini (2007). Kinematics of the Western Africa-Eurasia plate boundary from focal mechanisms and GPS data, *Geophys. J. Int.* **169,** 1180–1200.

Stramondo, S., M. Tesauro, P. Briole, E. Sansosti, S. Salvi, R. Lanari, M. Anzidei, P. Baldi, G. Fornaro, and A. Avallone (1999). The September 26, 1997 Colfiorito, Italy, earthquakes: Modeled coseismic surface displacement from SAR interferometry and GPS, *Geophys. Res. Lett.* **26,** 883–886.

Tao, W., T. Masterlark, Z. K. Shen, and E. Ronchin (2015). Impoundment of the Zipingpu reservoir and triggering of the 2008 M_w 7.9 Wenchuan earthquake, China, *J. Geophys. Res.* **120,** 7033–7047.

Tinti, E., L. Scognamiglio, A. Michelini, and M. Cocco (2016). Slip heterogeneity and directivity of the M_L 6.0, 2016, Amatrice earthquake estimated with rapid finite-fault inversion, *Geophys. Res. Lett.* **43,** doi: 10.1002/2016GL071263.

Trasatti, E., C. Kyriakopoulos, and M. Chini (2011). Finite element inversion of DInSAR data from the M_w 6.3 L'Aquila earthquake, 2009 (Italy), *Geophys. Res. Lett.* **38,** doi: 10.1029/2011GL046714.

Tung, S., and T. Masterlark (2016). Coseismic slip distribution of the 2015 M_w 7.8 Gorkha, Nepal, earthquake from joint inversion of GPS and InSAR data for slip within a 3-D heterogeneous domain, *J. Geophys. Res.* **121,** 3479–3503.

Turcotte, D., and G. Schubert (2014). *Geodynamics*, Cambridge University Press, Cambridge, United Kingdom.

U.S. Geological Survey (USGS) (2016). Summary poster of M 6.2 central Italy earthquake of 24 August 2016, in USGS National Earthquake Information Center, *U.S. Geological Survey.*

Valensise, G., P. Vannoli, R. Basili, L. Bonini, P. Burrato, M. M. C. Carafa, U. Fracassi, V. Kastelic, F. E. Maesano, and M. M. Tiberti (2016). Fossil landscapes and youthful seismogenic sources in the central Apennines: Excerpts from the 24 August 2016, Amatrice earthquake and seismic hazard implications, *Ann. Geophys.* **59,** doi: 10.4401/ag-7215.

Vasco, D. W., C. Wicks Jr., K. Karasaki, and O. Marques (2002). Geodetic imaging: Reservoir monitoring using satellite interferometry, *Geophys. J. Int.* **149,** 555–571.

Wang, H. F. (2000). *Theory of Linear Poroelasticity: With Applications to Geomechanics and Hydrogeology*, Princeton University Press, Princeton, New Jersey.

Wang, R., F. Lorenzo-Martín, and F. Roth (2006). PSGRN/PSCMP—A new code for calculating co- and post-seismic deformation, geoid and gravity changes based on the viscoelastic-gravitational dislocation theory, *Comput. Geosci.* **32,** 527–541.

Westaway, R. (1990). Present-day kinematics of the plate boundary zone between Africa and Europe, from the Azores to the Aegean, *Earth Planet. Sci. Lett.* **96,** 393–406.

Williams, C. A., and L. M. Wallace (2015). Effects of material property variations on slip estimates for subduction interface slow-slip events, *Geophys. Res. Lett.* **42,** 1113–1121.

Department of Geology and Geological Engineering
South Dakota School of Mines and Technology
MI 327A, 501 E. Saint Joseph Street
Rapid City, South Dakota 57701
sui.tung@sdsmt.edu
timothy.masterlark@sdsmt.edu

Manuscript received 2 May 2017;
Published Online 13 February 2018